Evidence for the Keplerian orbit of a close companion around a giant star

Mats Esseldeurs[1,⋆], Leen Decin[1,⋆], Joris De Ridder[1], Yoshiya Mori[2,3], Amanda I. Karakas[2,3,4], Jolien Malfait[1], Taïssa Danilovich[2,3,1], Stéphane Mathis[5], Anita M. S. Richards[6], Raghvendra Sahai[7], Jeremy Yates[8], Marie Van de Sande[9], Maarten Baes[10], Alain Baudry[11], Jan Bolte[12], Thomas Ceulemans[1], Frederik De Ceuster[1,13], Ileyk El Mellah[14,15,16], Sandra Etoka[6], Carl Gottlieb[17], Fabrice Herpin[11], Pierre Kervella[18], Camille Landri[1], Louise Marinho[19], Iain McDonald[6,20], Karl Menten[21,†], Tom Millar[22], Zara Osborn[2,3], Bannawit Pimpanuwat[23], John Plane[24], Daniel J. Price[2], Lionel Siess[25], Owen Vermeulen[1], Ka Tat Wong[26,27]

⋆ Corresponding authors. Emails: mats.esseldeurs@kuleuven.be; leen.decin@kuleuven.be.
† Passed away on 30/12/2024.

[1]*Institute of Astronomy, KU Leuven, Celestijnenlaan 200D, 3001 Leuven, Belgium*
[2]*School of Physics & Astronomy, Monash University, Clayton VIC 3800, Australia*
[3]*ARC Centre of Excellence for All Sky Astrophysics in 3 Dimensions (ASTRO 3D), Clayton 3800, Australia*
[4]*Kavli IPMU (WPI), UTIAS, The University of Tokyo, Kashiwa, Chiba 277-8583, Japan*
[5]*Université Paris-Saclay, Université Paris Cité, CEA, CNRS, AIM, 91191 Gif-sur-Yvette, France*
[6]*JBCA, Department of Physics & Astronomy, University of Manchester, Manchester, UK*
[7]*Jet Propulsion Laboratory, California Institute of Technology, Pasadena, CA 91109, USA*
[8]*University College London, Department of Computer Science, London, WC1E 6BT, UK*
[9]*Leiden Observatory, Leiden University, P.O. Box 9513, 2300 RA Leiden, The Netherlands*
[10]*Sterrenkundig Observatorium, Universiteit Gent, Krijgslaan 281 S9, 9000, Gent, Belgium*
[11]*Laboratoire d'Astrophysique de Bordeaux, Univ. Bordeaux, CNRS, B18N, allée Geoffroy Saint-Hilaire, 33615 Pessac, France*
[12]*Department of Mathematics, Kiel University, Heinrich-Hecht-Platz 6, 24118 Kiel, Germany*
[13]*Leuven Gravity Institute, KU Leuven, Celestijnenlaan 200D, 3001 Leuven, Belgium*
[14]*Departamento de Física, Universidad de Santiago de Chile, Av. Victor Jara 3659, Santiago, Chile*
[15]*Center for Interdisciplinary Research in Astrophysics and Space Exploration (CIRAS), USACH, Santiago, Chile*
[16]*Departament de Física, EEBE, Universitat Politècnica de Catalunya, Av. Eduard Maristany 16, 08019 Barcelona, Spain*
[17]*Harvard-Smithsonian Center for Astrophysics, 60 Garden Street, Cambridge MA 02138 USA*
[18]*LIRA, Observatoire de Paris, Université PSL, Sorbonne Université, Université Paris Cité, CY Cergy Paris Université, CNRS, 92190 Meudon, France.*
[19]*Instituto de Fisica Fundamental, CSIC, C/ Serrano 123, 28006 Madrid, Spain*
[20]*Open University, Walton Hall, Kents Hill, Milton Keynes MK7 6AA, UK*
[21]*Max-Planck-Institut für Radioastronomie, Auf dem Huügel 69,5 3121 Bonn, Germany*

[22] School of Mathematics and Physics, Queen's Universtity Belfast, Belfast BT7 1NN, UK
[23] National Astronomical Research Institute of Thailand, 260 Moo 4, Donkaew, Mae Rim, Chiang Mai 50180, Thailand
[24] School of Chemistry, University of Leeds, Woodhouse Lane, Leeds LS2 9JT, UK
[25] Institut d'Astronomie et d'Astrophysique and Brussels Laboratory of the Universe (BLU-ULB), Université libre de Bruxelles, CP 226, Boulevard du Triomphe, 1050 Brussels, Belgium
[26] Theoretical Astrophysics, Department of Physics and Astronomy, Uppsala University, Box 516, 75120 Uppsala, Sweden
[27] Institut de Radioastronomie Millimétrique, 38406 Saint-Martin-d'Hères, France

Close companions influence stellar evolution through tidal interactions, mass transfer, and mass loss effects. While such companions are detected around young stellar objects, main-sequence stars, red giants, and compact objects, direct observational evidence of close-in companions around asymptotic giant branch (AGB) stars has remained elusive. Here, we present (sub)millimeter time-domain imaging spectroscopy revealing the Keplerian motion of a close-in companion around the AGB star π^1 Gruis. The companion, slightly more massive than the AGB star, is likely a main-sequence star. Unlike more evolved stars with companions at comparable distances, π^1 Gru's companion follows a circular orbit, suggesting an eccentricity-generating mechanism late- or post-AGB. Our analysis suggests that model-predicted circularization rates may be underestimated. Our results highlight the potential of multi-epoch (sub)millimeter interferometry in detecting the Keplerian motion of close companions to giant stars and open avenues for our understanding of tidal interaction physics and binary evolution.

Main

Most stars with initial mass greater than 0.8 solar masses ($M_\odot$) probably host at least one planetary or stellar companion [1,2]. Of these stars, $\sim$95% will evolve through the Asymptotic Giant Branch (AGB) phase assuming a Salpeter initial mass function with exponent of 2.3 [3]. Companions with close orbits influence stellar evolution at all stages, shaping mass loss, altering envelope dynamics, and driving interactions that affect planetary nebula formation, extrinsic carbon star creation, and the recycling of enriched material into the interstellar medium [4–8].

Although close companions have been detected around a range of stars, from young stellar objects to main-sequence (MS) stars, red giants (RGB), white dwarfs (WD), and neutron stars [9–13], detecting companions in close orbits ($\lesssim$ 5 stellar radii) around AGB stars has proven difficult. AGB stars can undergo strong pulsations causing photometric variations of several magnitudes and shock velocities up to $\sim$10 km s^{-1}, extreme luminosities (up to 10^5 solar luminosities), and powerful winds with mass-loss rates ($\dot{M}$) from 10^{-8} to several times 10^{-5} $M_\odot$ yr^{-1} [14]. These conditions make transit and radial-velocity methods unsuitable for detecting close companions. While high-energy (UV/X-ray) emission suggests the presence of companions around AGB stars,

indicating associated accretion flows and disks [15], it does not reveal any orbital characteristics.

Long-term photometric monitoring of pulsating AGB stars reveals pulsation periods of hundreds of days, but in about a third of cases, a longer secondary period (LSP; 5–10 times the pulsation period) is detected, possibly indicating a companion's orbital period [16]. The LSP radial velocity amplitude can provide binary system properties only if it exceeds that of the stellar pulsation. In systems where the presence of a companion is independently confirmed, such as the red symbiotic binary CH Cyg [17], orbital parameters can be derived from the radial velocity curve. However, estimates of orbital eccentricity can be inaccurate owing to perturbations of the radial velocity by gas streams from the AGB star's extended atmosphere caught in the companion's gravitational potential. Moreover, only the mass function can be derived, and astrometric data is required to derive inclination and system masses. A combined radial velocity and astrometric analysis has been successfully applied only to the carbon-rich AGB star V Hya [18]. However, such analysis relies on narrow priors for primary mass and distance, and precise initial conditions for convergence. Moreover, this method cannot determine the barycentre's proper motion. In addition, since the companion is undetected, the nature of the LSP remains debated, with alternatives including plasma ejection, triple system dynamics, episodic dust formation, or convective oscillations [19,20]. Another approach has been explored for the red symbiotic R Aqr [21], where the companion's motion is inferred over time by assuming its position coincides with the centre of the H30α jet or the edge of the continuum emission, although only a single direct detection exists. Combining this assumed relative position with radial velocity measurements allows estimates of the system's orbital parameters.

The interaction between the AGB wind and potential companion(s) offers an alternative method for characterizing giant binary systems. Observations with the Atacama Large Millimeter/submillimeter Array (ALMA) have indirectly indicated the presence of companions to AGB stars through the detection of arcs, bipolar outflows, tori, rotating disks, and spirals in the otherwise smooth, radially outflowing wind [2]. However, unlike wide companions (e.g., Mira AB [22], W Aql [23]), no close companions have been directly detected in Keplerian motion through multi-epoch tracking of both components.

For two AGB stars, L_2 Pup and π^1 Gru, ALMA continuum data around 331.6 GHz and 241 GHz, respectively, reveal a maximum at the AGB star's position, plus an offset peak, potentially indicating a close companion [24,25]. Alternatively, the secondary peak may represent a dense aggregate of dust and gas formed by episodic mass loss, proposed as the cause of π^1 Gru's fast bipolar outflow [26]. Assuming the secondary peak in the ALMA π^1 Gru image traces a stellar companion orbiting an AGB star of mass $\sim$1.5 $M_\odot$, and approximating the tangential velocity anomaly by the orbital tangential velocity, it was inferred that this companion could be an accreting dwarf star of $\sim$0.86 $M_\odot$ on an eccentric ($e \sim 0.35$), $\sim$11-yr orbit[29]. The longevity (weeks to about a year) [24] and motion – Keplerian for a companion or radial for an outflowing aggregate – can help distinguish between these scenarios. To test this conjecture, we observed the AGB star π^1 Gru at high angular resolution ($\sim$0.″020) with ALMA during Cycle 6 (C6, June–July 2019, band 6, 241.0 GHz) and Cycle 10 (C10, October 2023, band 7, 334.7 GHz) (see 'ALMA observations' in

Methods).

Results

Direct evidence of the Keplerian motion of a close-in companion

In both ALMA C6 and C10 epochs, continuum data reveal two emission maxima (see Fig. 1, Extended Data Fig. 1 and Extended Data Table. 1). The relative position of the secondary peak (referred to as M_2) with respect to the AGB star (M_1) was measured in right ascension ($\alpha_\star$) and declination (δ) as $(-12.0 \pm 1.2, -34.7 \pm 1.2)$ mas in the C6 data, and $(-24.1 \pm 0.7, 32.9 \pm 1.0)$ mas in the C10 data (see 'ALMA observations' in Methods). This positional shift is inconsistent with pure radial motion, but can be explained by an elliptical orbital projection, as expected from Newtonian gravitational interaction between two masses (see 'Orbital parameters' in Methods). This marks the direct detection of the Keplerian motion of a close-in companion around an AGB star, confirming the earlier hypothesis of the presence of a close-in companion around π^1 Gru [25,27–29]. π^1 Gru also has a distant G0V companion, π^1 Gru B, at a projected separation of $2\farcs71$, known since 1953 [30]. This confirms π^1 Gru as a hierarchical triple system, consisting of a close-in companion (π^1 Gru C) and a widely separated tertiary companion, which is unlikely to significantly influence the inner binary's dynamics (see 'Orbital parameters' in Methods).

System's orbital motion and barycentre's proper motion

Combining the multi-epoch ALMA proper motion images with *Hipparcos* and *Gaia* position-velocity vectors from epochs 1991.25 and 2016.0 (see Fig. 1), we assembled data spanning nearly 25 years. Using 18 observational constraints, including astrometric positions, velocities, and parallax, we solved the two-body problem under Newtonian gravity and determine both the system's orbital motion and the barycentre's proper motion.

The proper motion vector is defined by six orbital elements (Ω, i, ω, a, e, T_0), along with π^1 Gru A's mass (m_1), the mass ratio ($q = m_2/m_1$, with m_2 the mass of M_2), the barycentre's proper motion (μ_α^G, μ_δ^G), and parallax (ϖ, or distance D). Here, Ω is the longitude of the ascending node, i inclination, ω argument of periastron, a semi-major axis, e eccentricity, and T_0 time of periastron passage. Using Bayesian inference, we derived posterior distributions for these 11 parameters. Broad, agnostic priors were adopted except for distance, which followed a Gamma prior. Geometrical degeneracies were present, with i degenerate with $360^\circ - i$ and (ω, Ω) degenerate with their antipodal values $(\omega + 180^\circ, \Omega + 180^\circ)$, but resolved using ALMA spectral line data (see 'Orbital parameters' in Methods).

Specifically, we derive that $m_1 = 1.12 \pm 0.25\,\mathrm{M}_\odot$, $q = 1.05 \pm 0.05$, $a = 6.81 \pm 0.49$ au, $\Omega = 101 \pm 36^\circ$, $i = 11 \pm 7^\circ$, $D = 179.74 \pm 10.09$ pc, $\mu_\alpha^G = 45.203 \pm 0.144$ mas yr^{-1}, and $\mu_\delta^G = -18.76 \pm 0.061$ mas yr^{-1} where the analysis strongly favors a circular orbit; see corner plot

in Extended Data Fig. 2. The fit to the proper motion data is shown in Fig. 1 and Suppl. Video 1; the orbital system is visualized in Extended Data Fig. 3. With a more informed Gaussian prior on m_1 with mean $1.5\pm0.5\,\mathrm{M}_\odot$, the retrieved m_1 increases to $1.27\pm0.22\,\mathrm{M}_\odot$ (see 'Orbital parameters' in Supplementary Information), remaining within the uncertainty interval of our initial determination.

We derive the barycentre's radial velocity as $-14.8 \pm 1.0\,\mathrm{km\,s^{-1}}$ (see 'Orbital parameters' in Methods). Using the celestial coordinates, and derived distance, proper motion, and radial velocity, we determined the system's 6D Galactocentric phase-space position. By back-integrating its orbit over 2.8 Gyr, we find that the π^1 Gru system likely formed near the Galactic plane, close to or slightly within the Solar orbit (see 'Galactic orbit' in Supplementary Information).

Nature of π^1 Gru C and its accretion disk

We deduce that the companion orbits the AGB star in an anti-clockwise direction and is surrounded by an accretion disk. An SED analysis indicates that π^1Gru C is either an F6–F8V MS star or a massive WD with a temperature up to 40,000 K, with additional (sub)millimeter emission from an accretion disk interacting with the companion. The UV emission is either intrinsic, from the AGB star's chromosphere, or extrinsic, suggesting ongoing but weak accretion (see 'Accretion disk' in Supplementary Information).

Wind Roche lobe overflow (RLOF) [31] shapes the AGB circumstellar envelope's density structure and the accretion disk around the companion (see 'Hydrodynamical modelling' in Methods). To estimate the mass accretion rate and investigate the accretion disk's characteristics, we perform high-resolution hydrodynamic simulations [32,33] (see 'Hydrodynamical modelling' in Methods). The resulting density distribution (Extended Data Fig. 4) shows a bow shock spiral in front of a dense, circular accretion disk with an outer radius of ∼0.83 au. The disk material orbits with tangential velocities of 80–100% of the Keplerian velocity and is flared in the edge-on view, with a density scale height of ∼0.15 au at the outer radius. The mass accretion is ∼15% of the mass loss rate ($8 \times 10^{-7}\,\mathrm{M}_\odot\,\mathrm{yr}^{-1}$ [26]), corresponding to a mass accretion rate of $1.2 \times 10^{-7}\,\mathrm{M}_\odot\,\mathrm{yr}^{-1}$, and the disk's total mass is $2 \times 10^{-6}\,\mathrm{M}_\odot$. ALMA band 6 and 7 at π^1 Gru C's position gives us a spectral index of $\alpha^s_{M_2} = 2.3 \pm 0.3$ ($F_\nu \propto \nu^{\alpha^s}$), indicating dust dominance [34]. For the accretion disk to account for this emission, the estimated disk dust mass is $\sim 8.5 \times 10^{-8}\,\mathrm{M}_\odot$ (see 'Hydrodynamical modelling' in Methods).

System's initial configuration and future evolution

Using stellar evolution calculations [35], we estimate the initial mass of π^1 Gru A. The core-mass luminosity diagram and the observed C/O ratio indicate a best-fit initial mass of $1.7\,\mathrm{M}_\odot$, with bounds of $1.25\,\mathrm{M}_\odot$ and $2\,\mathrm{M}_\odot$ (see 'Stellar evolution' in Methods). As an additional constraint, we analyzed π^1 Gru A's pulsation characteristics. Classified as an SRb long-period variable, π^1 Gru A has a pulsation period of ∼195 days [36], which we attribute to the radial first overtone mode (see 'Stellar evolution' in Methods; Extended Data Fig. 5). Stellar evolution models [35] combined with

linear pulsation calculations [37] indicate that the observed period and luminosity are consistent with an initial mass of $1.5-2\,M_\odot$. For an initial mass of $1.7\,M_\odot$, the model predicts a current mass of $\sim$1.4 $M_\odot$, near the end of the thermally pulsating (TP)-AGB evolution. Growth rates further confirm that the first overtone mode can dominate even during late thermal pulses (see Fig. 2). Thus, despite its advanced TP-AGB age, π^1 Gru A remains a semi-regular variable rather than transitioning to a Mira variable pulsating in the fundamental mode. The TP-AGB mass estimate of $\sim$1.4 $M_\odot$ lies at the upper limit of the m_1 agnostic prior retrieval, being more compatible with the Gaussian prior.

The current system parameters allow us to reconstruct the past and predict the future of the π^1 Gru inner binary through orbital evolution calculations. The survival of close companions depends on the balance between tidal forces, mass loss, and mass transfer. We account for non-conservative mass transfer by incorporating it into the orbital angular momentum balance equation. Additionally, we include both equilibrium and dynamical tide dissipation, with the latter incorporating the excitation and dissipation of progressive internal gravity waves in evolved stars [8] (see 'Orbital evolution' in Methods).

Our orbital evolution calculations reveal that the π^1 Gru system parameters remained relatively unchanged during the main-sequence and horizontal branch phases (Fig. 3). The orbit began to expand modestly during the RGB phase, driven by mass loss from the primary star. However, during the TP-AGB phase, the interplay of non-conservative mass transfer and enhanced tidal dissipation caused significant orbital contraction, which will eventually lead to a common envelope phase. Mass loss from π^1 Gru A and accretion onto π^1 Gru C shifted the mass ratio from $q < 1$ to $q > 1$ (Fig. 3d). In the WD scenario, there remains a small probability that the system could explode as a Type Ia supernova, potentially allowing the system to avoid a common-envelope fate due to a WD kick.

Discussion

Close giant binaries with orbital periods $T_{\rm orb} \lesssim$ 4,000 days are expected to circularize through tidal dissipation [38]. This is supported by our refined tidal models tailored to the specific configurations of π^1 Gru. Specifically, we derive that higher eccentricities result in faster circularization rates and that the circularization mainly occurs at the very end of the TP-AGB phase (see 'Orbital evolution' in Methods and Extended Data Fig. 6). Thus, the detection of an AGB binary with a circular orbit and $T_{\rm orb} \sim 11.76$ years ($\sim$4,295 days) might appear unsurprising. However, this contrasts with post-AGB binaries, where systems with $T_{\rm orb} \gtrsim$ 1,000 days are observed to be exclusively eccentric, creating a discrepancy between theory and observations [39].

Two main hypotheses address this discrepancy. The first suggests incomplete knowledge of tidal dissipation: tidal circularization rates may be underestimated for the (progenitor) solar-type main-sequence binaries [40], while overestimated during the giant phase for ellipsoidal red giant binaries [41]. We add a single, critical data point to this discussion: confirmation that a TP-AGB binary system is circularized at $T_{\rm orb} >$ 1,000 days. It tentatively favors the second hypothesis:

a mechanism generating eccentricity at the end of the TP-AGB or during the post-AGB phase. Proposed mechanisms include mass transfer at periastron, asymmetric mass loss, interactions with a circumbinary disk, white-dwarf kicks, hybrid wind-RLOF mass transfer, or the eccentric Kozai-Lidov mechanism in triple systems [38,39]. Future studies of AGB binary systems may allow a sampling of the $e - \log T_{\rm orb}$ distribution, providing critical evidence to this discussion.

Our results also constitute an important test for tidal interaction physics. A key inference is that our orbital evolution models predict minimal change in the binary's eccentricity, implying an initially near-circular orbit since the system is currently circular (see Extended Data Fig. 6). Combined with the observed large eccentricities and deficit of systems with $e < 0.15$ among main-sequence solar-type binaries with orbital periods above 10 days [1], this may suggest that our circularisation rates are underestimated. This tension between theory and observations is reinforced by a recent study of red giant binary eccentricities [42]. One potential avenue for investigation is resonance locking, a phenomenon where the tidal forcing frequency and the frequency of a stellar pulsation mode vary in concert, enabling sustained resonant interactions over extended timescales compared to scenarios where either of these frequencies were constant [43].

Alternatively, π^1 Gru's inner binary system may have already undergone circularization, which would lend support to the hypothesis that π^1 Gru C evolved already through the AGB phase and is now a WD. However, post-AGB binary systems with WD companions – such as extrinsic S-type stars, barium stars, red symbiotics and WD-MS systems – are all observed to have non-circular orbits across orbital periods ranging from ∼1,000 – 10,000 days [39]. If the eccentricity-generating mechanism proposed for these systems applied here, it must have been unusually weak or inactive to result in the observed low eccentricity of the WD-AGB phase.

Moreover, using the WD mass distribution function derived from *Gaia* data [44], the probability of π^1 Gru C being a massive WD, with mass $1.18 \pm 0.27\,{\rm M}_\odot$, is only ∼3%. Such massive WDs are thought to form through the merger of two average-mass WDs in close binaries or from the evolution of massive intermediate-mass single stars [44]. Massive WDs accreting at the rate inferred here ($\sim 1.2 \times 10^{-7}$ M$_\odot$ yr^{-1}) are present in symbiotic recurrent novae, whose optical and UV spectra show strong H I, He I, and He II emission lines [45], none of which are observed toward π^1 Gru. Furthermore, the accreting companion was not detected with SPHERE-ZIMPOL [46], whereas the accreting WD in R Aqr was detected by the same instrument despite an order of magnitude lower accretion rate [47]. These statistical and observational constraints make it more likely that π^1 Gru C is a MS star in a primordial circular orbit.

Hence, neither evolutionary scenario for π^1 Gru C is without tension. Future spectrally resolved UV observations with the *Hubble Space Telescope* may reveal the nature of the companion, with narrower line profiles pointing to a MS star, while broader profiles would be more indicative of a WD [15].

This study presents the direct detection of the Keplerian motion of a close-in companion around an AGB star. By combining multi-epoch (sub)millimeter imaging with optical astrometric data, we achieve precise proper motion fitting, disentangling the barycentre's motion from the bi-

nary's orbital dynamics. The retrieved orbital parameters provide a crucial benchmark for stellar and binary evolution models, revealing tensions in tidal interaction physics. This work shows the potential of future multi-epoch (sub)millimeter imaging, particularly when combined with *Gaia* DR4's optical astrometry, to derive orbital constraints for giant binaries and improve our understanding of the tidal interactions and orbital transformations governing the evolution of stars, which commonly reside in binary systems.

Methods

1. ALMA observations

1.1. Observations

π^1 Gru was observed at high resolution as part of ALMA project codes 2018.1.00659.L and 2023.1.00091.S, during Cycle 6 (June 23 and July 6, 2019, Band 6, central frequency 241 GHz) and Cycle 10 (October 12 and October 26, 2023, Band 7, central frequency 334 GHz), respectively. In 2019, π^1 Gru was also observed in two other lower-resolution ALMA configurations, as described in ref. [48]. The observations were made in multiple, non-contiguous spectral windows (spw) at an initial spectral resolution $\sim$ 1 MHz or finer. The data from each epoch were combined and are referred to as C6 and C10 data throughout this work. The 2019 observations and data reduction process are detailed in Ref. [48]. Only the extended configuration data are used for continuum analysis here. For the 2023 data, a similar method was employed, with the main difference being the use of a higher frequency and smaller frequency span $\Delta\nu$. J2230-4416 and J2235-4835 served as phase reference sources, while J2242-4204 and J2230-4416 were used as check sources in 2019 and 2023, respectively. The check source, a compact source at a comparable angular separation from the phase reference as the target, was observed occasionally as if it were a target. The angular separations (in right ascension $\alpha_\star$ and declination δ) of the check source and target from the phase reference are denoted by $\psi_{\rm check}$ and $\psi_{\rm targ}$, respectively. In both cases, the maximum recoverable scale (MRS) is larger than the region containing the π^1 Gru system. Details are summarized in Supplementary Table 1. The principal data products are continuum images of the system, analysed in this paper, and spectral line cubes, of which only the CO, SiO, and SiS data are used here.

1.2. Calibration and imaging

In brief, we began with the target data after applying the ALMA pipeline calibration (excluding the pipeline self-calibration available in 2023). We identified line-free channels from the pipeline images for the 2019 data, and from the calibrated visibilities in 2023. Here, $\Delta\nu$ represents the cumulative bandwidth of line-free channels distributed across $\nu_{\rm tot}$, and $\nu_{\rm mean}$ denotes the mean frequency of the line-free continuum channels. For each epoch, we made channel-averaged copies

of the phase-referenced target data. These were used to create continuum images, excluding line emission, (from all data in 2019 and from the first execution with the best signal-to-noise ratio (S/N) in 2023), as starting models for phase and amplitude self-calibration. The system's proper motion is $\sim$1 mas during the 2-week interval between observations at each epoch; the self-calibration aligned the image peak with the positions given on the dates provided in Supplementary Table 1 for C6 and C10, respectively, i.e. the mean date for C6 and the date of the first execution for C10.

The array configuration used in 2019 provided slightly longer baselines relative to observing wavelength than in 2023. In order to provide images with similar synthesized beam sizes ($\theta_{\rm b}$) we weighted the data during imaging, using robust parameter values of +0.5 in 2019 and -0.5 in 2023; the beams are within 5% of circular, hence the geometric mean sizes are quoted here. Supplementary Table 1 summarizes the main continuum imaging parameters, including the off-source noise $\sigma_{\rm rms}$. The ALMA C6 2019 and ALMA C10 2023 continuum images are displayed in Extended Data Fig. 1.

The target data at full spectral resolution were adjusted to constant velocity ($v_{\rm LSRK}$) in the direction of π^1 Gru. We applied the continuum self-calibration solutions to these data and subtracted the continuum before making spectral image cubes for each spw. Here, we use measurements from 2019 extended-configuration cubes only, with an angular resolution of $\sim 0\farcs023$ and a noise rms in quiet channels of 0.9–1.4 mJy, increasing with frequency; full details are tabulated in ref. [48]. The details of the 2023 spectral cubes are given in Supplementary Table 2, including the synthesised beam sizes achieved with robust +0.5 in order to optimise sensitivity to extended molecular emission. In some cases, cubes were made at two spectral resolutions; at the highest resolution for masers and with channel averaging for thermal lines, and at higher angular resolution, robust -0.5 for SiO and CO v=1 J=3-2 shown in Supplementary Fig. 8. The positions and flux densities of maser spots at both epochs were measured by fitting 2-D Gaussian components in the AIPS package (task `SAD`); the position errors were estimated as described in Section 1.3.1, in the range 1 – 10 mas depending on S/N. The transitions used in this paper are listed in Supplementary Table 3.

1.3. Measurements of ALMA continuum sources

We measured the positions of the primary (π^1 Gru A, hereafter referred to as M_1) and the nearby companion (π^1 Gru C, hereafter referred to as M_2) in two ways: using the CASA task `imfit` to fit two 2-D Gaussian components to M_1 and M_2 and using the `uvmultifit` add-on package [49] to fit a uniform disc (UD) plus a delta (point-like) component to the calibrated visibilities. For both epochs and methods we allowed the fit to M_1 to be elliptical with the ratio of major and minor axes $e_{\rm r} \geq 0.9$, (where $e_{\rm r} = 1$ is a perfect circle). We assumed that M_2 is unresolved as its relative faintness and proximity to M_1 rendered attempts to measure a size based on formal S/N errors (Section 1.3.1) unreliable, and therefore specified a point source.

1.3.1 Stochastic and other relative measurement errors

The errors reported by the packages are based on the assumption that the source can be described exactly by the model and on ideal phase noise, and tend to underestimate realistic errors. In fact these errors are 'formal errors' reported by the packages; they are not 'absolute errors' which may include systematic effects not fully calibrated. The relative position uncertainty due to phase noise in a Gaussian fit to an interferometry image from an array with gaps in the baseline coverage (as for ALMA in the extended configuration) is given by $\sigma_{\mathrm{pos},\phi} = \theta_{\mathrm{b}} \times \sigma_{\mathrm{rms}}/P$ where P is the fitted peak flux density. The two methods gave results within 1 mas for the relative positions of the components (although as expected, the FWHM of the Gaussian component for component M_1 underestimates the stellar size). It is likely that a UD is a better fit to the stellar continuum at (sub)millimeter wavelengths as visibility-plane fitting is not affected by deconvolution errors — although still potentially biased by blending of the components at the interferometer resolution and emission which is not included in the UD plus delta model. Any deviations of the apparent stellar shape from a circle are in reality not likely to be elliptical but random (due to stellar activity, localised mass loss, dust clumps etc.) on scales large enough not to average into noise. We therefore adopt the UD plus delta model, utilizing the phase noise estimate (where P is calculated as the UD flux density multiplied by the ratio of the beam area to the UD area) and the ellipticity to estimate the errors.

The provisional relative position uncertainties σ_{prov} are taken as the sum in quadrature of $\sigma_{\mathrm{pos},\phi}$ and, for component M_1, the error due to the assumption of ellipticity. We estimated the latter as $\sigma_{\mathrm{pos,e_r}}$ = (fitted diameter)$\times(1 - e_{\mathrm{r}}) \times \sqrt{2}$. σ_{prov} thus represents the errors in UD plus delta visibility plane fitting, including phase noise. We then compared the positions obtained by visibility plane fitting with those from Gaussian fitting in the image plane, giving their differences in each direction, $\sigma_{\mathrm{pos,fit}}$. σ_{prov} and $\sigma_{\mathrm{pos,fit}}$ are decomposed into equal components in $\alpha_\star$ and δ, considering that the synthesized beams are nearly circular and the other uncertainties have unknown orientations.

We then took the larger of σ_{prov} or $\sigma_{\mathrm{pos,fit}}$ as the actual relative position uncertainty $\sigma_{\mathrm{pos,rel}}$. $\sigma_{\mathrm{pos,fit}}$ was larger only for component M_2 in 2023, probably due to slightly lower resolution and brighter dust. These values are listed in Extended Data Table 1 and can be used to determine the uncertainty in the separation of the two components at each epoch.

The astrometric positions of M_1 and M_2 at both ALMA epochs are listed in Extended Data Table 1 and visualised in Extended Data Fig. 1. The relative position of M_2 with respect to M_1 was measured as ($\alpha_\star$, δ) = (-12.025 ± 1.212, -34.700 ± 1.212) mas in the ALMA 2019 C6 data and as (-24.103 ± 0.721, 32.910 ± 1.000) mas in the ALMA 2023 C10 data. Consequently, the angular separation between M_1 and M_2 changed from -37.702 ± 1.898 mas in 2019 to 40.775 ± 1.233 mas in 2023. This positional shift is inconsistent with pure radial motion.

The measured UD diameters D_{UD} of M_1 and the flux densities of both components, S_{UD} and S_{delta}, are given in Supplementary Table 4. We estimate the error σ_{UD} from the same phenomena

as those causing $\sigma_{\rm pos,rel}$, given in Extended Data Table 1, using the combined $\alpha_\star$ and δ errors, with an additional factor of $\sqrt{2}$ as the diameter is the difference between two position measurements. The relative continuum flux density errors in $S_{\rm UD}$ and $S_{\rm delta}$ are similar at each epoch, comprising the noise $\sigma_{\rm rms}$ and fitting uncertainties, shown as $\sigma_{\rm S}$. When comparing the two epochs, the ALMA flux scale error, typically 7% at these frequencies [50], should also be included. Using $\nu_{\rm mean}$ from Supplementary Table 1, the spectral index, α^s of each component (ignoring any potential variability) is $\alpha^s_{M_1} = 1.9 \pm 0.3$ and $\alpha^s_{M_2} = 2.3 \pm 0.3$ (using the convention $S \propto \nu^{\alpha^s}$).

1.3.2 Astrometric uncertainty

The absolute astrometric accuracy is determined by use of the phase reference source. The main contributions to astrometric errors are the phase reference position errors $\sigma_{\rm phref}$, short-term phase jitter within each few-minute scan $\sigma_{\rm short}$, and errors in transferring phase solutions from the phase reference source to the target $\sigma_{\rm trans}$. We took $\sigma_{\rm phref}$ from the ALMA calibrator catalogue. $\sigma_{\rm short} = \theta_{\rm b} \times \phi_{\rm rms}/360$, where the phase rms $\phi_{\rm rms}$ in degrees was taken from the QA0 reports (for the best observation at each epoch) [50]. $\sigma_{\rm trans}$ is dominated by antenna position errors and by atmospheric differences between the directions of the sources, which we assume to be equivalent to a phase screen with a linear gradient. We estimated the effect on the target by comparing the apparent and catalogue positions of the check source to derive its error ($\sigma_{\rm pos,check}$) and scaling these to the phase calibrator - target separation, $\sigma_{\rm pos,scaled} = \sqrt{(\sigma^2_{\rm pos,check} + \sigma^2_{\rm short})} \times (\psi_{\rm targ}/\psi_{\rm check})$ (from Supplementary Table 1). The target astrometric (absolute) uncertainty is then given by $\sigma_{\rm pos,abs} = \sqrt{\sigma^2_{{\rm pos},\phi} + \sigma^2_{\rm pos,scaled} + \sigma^2_{\rm short}}$. The values are given in Supplementary Table 5. We use more significant figures than are strictly warranted in order to avoid rounding errors in later modelling.

The check source catalogue position uncertainties are $\sim$1–2 mas. However, without a comprehensive directional atmospheric model (i.e., multiple calibrators), it is not realistic to include these uncertainties, as their contribution would be minor.

2. Orbital parameters

In order to determine the orbital parameters of the close-in companion, π^1 Gru C, we will first introduce the orbital model, followed by a description of the observational constraints obtained from the ALMA, *Gaia*, and *Hipparcos* data. We will then describe the Bayesian analysis used to derive the orbital parameters. Finally, a sensitivity analysis is performed to assess the robustness of the derived orbital parameters.

2.1. Orbital model

The 2019 ALMA Cycle 6 continuum data revealed two maxima separated by 37.702 mas, with the secondary peak interpreted as a potential close companion [25]. However, this feature could also be a dense clump of gas and dust resulting from a mass ejection from the AGB star, which would follow a more radial outflow. The 2023 ALMA Cycle 10 data provide a second epoch to confirm the proper motion, definitively ruling out the possibility of a radially outflowing aggregate. Instead, the positional shift observed in the 2023 C10 data is consistent with an elliptical projection on the sky, thereby establishing that the secondary continuum peak is a close-in companion on a Keplerian orbit around the AGB star. This confirms the hypothesis of Ref. [25,27–29] that a close-in companion interacts with the wind of π^1 Gru A. However, their study lacked the observational constraints necessary to determine the orbital parameters accurately.

Since 1953, it is already known that π^1 Gru has another far distant G0V companion, π^1 Gru B, at a projected separation of $2\farcs71$ [30]. This establishes π^1 Gru as a triple system. The dynamical evolution of triple systems with a close-in binary and a wider tertiary may be influenced by the 'Eccentric Kozai-Lidov' (EKL) mechanism [51,52], which can cause the inner binary to experience large-amplitude oscillations in eccentricity and inclination, driving it to small pericentre distances and potential merger, while the tertiary may move outward or become unbound over evolutionary timescales. On one hand, it has been demonstrated that for a circular inner orbit, a large mutual inclination ($40^\circ - 140^\circ$) can lead to long-timescale modulations that drive the eccentricity to very high values and can even result in orbital flips [53]. Although we will derive the inclination of the inner orbit below, the inclination of the outer orbit (of π^1 Gru B) is currently unconstrained, preventing an accurate assessment of the EKL effect for a potentially high mutual inclination.

On the other hand, it has been shown that even starting with an almost coplanar configuration, for eccentric inner and outer orbits, the inner orbit's eccentricity can still be excited to high values, and the orbit can flip by approximately 180°, rolling over its major axis [53]. However, as shown below, we derive a circular orbit for the inner orbit (of π^1 Gru C), suggesting that the EKL mechanism is not active here.

Even without considering the EKL mechanism, it is necessary to evaluate the effect of the distant companion on the orbital motion of the two inner bodies due to Newtonian gravitational interactions. This distant companion, with a mass of $\sim$1 $M_\odot$, exerts a negligible influence on the orbital motion of the two inner bodies. Over a span of 24.25 years, the maximum induced change in the astrometric position of the inner bodies due to π^1 Gru B is only about 0.65×10^{-5} mas. Consequently, we can model the astrometric motion of the primary AGB star, π^1 Gru A (M_1), and its inner companion, π^1 Gru C (M_2), as a two-body system, effectively neglecting the influence of π^1 Gru B.

We therefore model the orbital motion of the two celestial bodies, M_1 and M_2, in a binary system using Newton's laws, aiming to determine their positions over time, t, while accounting for

parallax, proper motion, and orbital parameters. This involves analyzing the motion of M_1 and M_2 interacting solely through their mutual gravitational attraction.

The remainder of the derivation of the orbital equations, including the explicit transformation from the orbital plane to the plane of the sky, the calculation of the true anomaly as a function of time, and the projection of the orbital motion onto the observed astrometric coordinates, is detailed in Supplementary Sect. 2.1. This section provides the full mathematical framework required to compute the predicted positions of both components at any given epoch, accounting for the effects of parallax, proper motion, and the orientation of the orbit in three-dimensional space. The derivation also discusses the conventions adopted for the orbital elements and clarifies the treatment of degeneracies in inclination and node, ensuring that the model predictions can be robustly compared to the multi-epoch astrometric data from ALMA, *Gaia*, and *Hipparcos*.

2.2. Observational input

The orbital parameters for π^1 Gru, as defined in Supplementary Sect. 2.1, can be constrained using data from ALMA C6, ALMA C10, *Gaia* DR3, and *Hipparcos*, along with their respective uncertainties.

The ICRS astrometric positions of component M_1 and M_2 at the epoch of the ALMA C6 and C10 observations are listed in Extended Data Table 1. The positional accuracy is given by $\sqrt{\sigma^2_{\rm pos,rel} + \sigma^2_{\rm pos,abs}}$. These ALMA positions are not yet corrected for the parallactic shift since the parallax ϖ is one of the retrieval parameters.

To summarize, for the ALMA C6 data:

$$\alpha_{\rm C6}(M_1) = 22^h22^m44.269589^s \pm 0.000240^s \quad \text{(OC1)}$$
$$\delta_{\rm C6}(M_1) = -45^\circ56'53.00641'' \pm 0.001697'' \quad \text{(OC2)}$$
$$\alpha_{\rm C6}(M_2) = 22^h22^m44.268393^s \pm 0.000212^s \quad \text{(OC3)}$$
$$\delta_{\rm C6}(M_2) = -45^\circ56'53.04198'' \pm 0.001217'' \quad \text{(OC4)}$$

For the ALMA C10 data:

$$\alpha_{\rm C10}(M_1) = 22^h22^m44.282263^s \pm 0.000200^s \quad \text{(OC5)}$$
$$\delta_{\rm C10}(M_1) = -45^\circ56'53.12381'' \pm 0.001777'' \quad \text{(OC6)}$$
$$\alpha_{\rm C10}(M_2) = 22^h22^m44.279952^s \pm 0.000196^s \quad \text{(OC7)}$$
$$\delta_{\rm C10}(M_2) = -45^\circ56'53.09090'' \pm 0.001612'' \quad \text{(OC8)}$$

Although the components of the binary system are not resolved in the *Gaia* and *Hipparcos* data, the fact that the companion remains undetected in the VLT/SPHERE data [46] taken contem-

poraneously with the ALMA C6 data (see Supplementary Sect. 5.2), implies that the mass-to-light ratios of π^1 Gru A and π^1 Gru C are significantly different, and that the *Hipparcos* and *Gaia* photocenters therefore track the photocentre of the AGB star M_1. The *Hipparcos* catalogue (https://www.cosmos.esa.int/documents/532822/552851/vol9_all.pdf/50682119-3f37-4048-8f3a-e10961614b44) lists the following five-dimensional (5D) (the radial velocity could not be constrained from the *Hipparcos* and *Gaia* measurements) ICRS position-velocity vector for π^1 Gru (= HIP 110478) at epoch 1991.25:

$$\boldsymbol{y}_{\mathrm{Hip},M_1} = \begin{pmatrix} \alpha^* \\ \delta \\ \varpi \\ \mu_{\alpha^*} \\ \mu_\delta \end{pmatrix}_{M_1} = \begin{pmatrix} 233.40516824561706 \\ -45.94791727 \\ 6.54 \\ 27.89 \\ -10.92 \end{pmatrix}_{\mathrm{Hip}} \qquad \text{(OC9)–(OC13)}$$

Both α^* and δ are expressed in degrees, the *Hipparcos* parallax ϖ is expressed in milli-arcseconds (mas), and the proper motions μ_{α^*} and μ_δ are expressed in mas yr^{-1}. The corresponding covariance matrix Σ_{Hip} is

$$\Sigma_{\mathrm{Hip}} = \begin{pmatrix} 0.64 & 0.0496 & -0.0808 & -0.17952 & -0.08528 \\ 0.0496 & 0.3844 & -0.15655 & -0.12648 & -0.172856 \\ -0.0808 & -0.15655 & 1.0201 & 0.236946 & 0.132512 \\ -0.17952 & -0.12648 & 0.236946 & 1.0404 & 0.25092 \\ -0.08528 & -0.172856 & 0.132512 & 0.25092 & 0.6724 \end{pmatrix} \qquad (1)$$

where the uncertainties of α^*, δ, and ϖ are expressed in mas.

The *Gaia* DR3 archive [54] lists the following astrometric solution for π^1 Gru (=*Gaia* DR3 6518817665843312000) at epoch 2016.0:

$$\boldsymbol{y}_{\mathrm{Gaia},M_1} = \begin{pmatrix} \alpha \\ \delta \\ \varpi \\ \mu_{\alpha^*} \\ \mu_\delta \end{pmatrix}_{M_1} = \begin{pmatrix} 335.6844004512271 \\ -45.94804349249061 \\ 6.185845810192854 \\ 31.105558619539813 \\ -10.338212763867 \end{pmatrix}_{\mathrm{Gaia}} \qquad \text{(OC14)–(OC18)}$$

where the units are the same as for the *Hipparcos* solution. The corresponding covariance matrix Σ_{Gaia} is:

$$\Sigma_{\mathrm{Gaia}} = \begin{pmatrix} 0.05428154 & 0.01727978 & 0.00399398 & 0.01529596 & -0.01802598 \\ 0.01727978 & 0.0856448 & -0.02478438 & -0.0093199 & -0.03776861 \\ 0.00399398 & -0.02478438 & 0.19944953 & -0.02224772 & -0.05414651 \\ 0.01529596 & -0.0093199 & -0.02224772 & 0.06329501 & 0.02410661 \\ -0.01802598 & -0.03776861 & -0.05414651 & 0.02410661 & 0.12071868 \end{pmatrix} \qquad (2)$$

where the units are the same as for Σ_{Hip}.

These 18 observational constraints, (OC1)–(OC18), will be used to infer the 6 orbital parameters (a, e, Ω, i, ω and T_0), the primary mass m_1, the mass ratio $q = m_2/m_1$, the parallax ϖ toward the π^1 Gru system (or, equivalently, its distance D), and the proper motion vector of the barycentre $\boldsymbol{\mu}^G$.

2.3. Predictables

The 18 observational constraints (OC1) – (OC18) are compared with 18 predicted values to derive the orbital parameters of the π^1 Gru system. Specifically, we fit the astrometric positions and parallax shift of M_1 and M_2 at the ALMA C6 and C10 epochs, and fit the astrometric positions, parallax and proper motion of M_1 from the *Hipparcos* and *Gaia* epochs.

We have intentionally left the ALMA observations uncorrected for the parallactic shift, as this shift depends on parallax, one of the parameters in the Bayesian retrieval fitting. To correctly apply Bayes' theorem, a clear distinction between observables and predictables must be maintained, avoiding any mixing between them. Once the parallax has been determined in a way that is consistent with the ALMA, *Hipparcos*, and *Gaia* data, the ALMA observations can be corrected for the parallactic shift and only the motion fits including the proper motion and orbital motion can be displayed. Accordingly, all figures in this paper displaying proper motion fits have been constructed after applying this approach.

It is important to note that the observed proper motion derived from *Gaia* and *Hipparcos* represents an average value over the duration of each mission. The *Hipparcos* mission lasted from 1989.8 to 1993.2, while the *Gaia* mission spanned from 2014.5 to 2017.4. The timestamps for the *Gaia* observations of π^1 Gru are readily available and were used to derive the mean proper motion of M_1 for the *Gaia* epoch. However, the exact timestamps for the *Hipparcos* mission could not be retrieved. To address this, we sampled *Hipparcos*' full observational time span with 300 linearly spaced timestamps, which were then used to calculate the right ascension and declination of M_1 at each timestamp, and hence to derive the average proper motion for the *Hipparcos* epoch. Sampling with more data points did not impact the results. Additionally, given that the *Hipparcos* data have a limited impact on the overall results, as demonstrated in the sensitivity analysis presented in Supplementary Sect. 2.3.2, this assumption is considered well justified.

2.4. Baysesian inference

Using the Bayesian framework, we compute the posterior distribution $P(\boldsymbol{\theta} \mid \boldsymbol{y})$ which is proportional to the product of the likelihood function and the prior distribution:

$$P(\boldsymbol{\theta} \mid \boldsymbol{y}) \propto P(\boldsymbol{y} \mid \boldsymbol{\theta})\, P(\boldsymbol{\theta}). \tag{3}$$

where $\boldsymbol{\theta} = (m_1, q, a, e, T_0, \omega, \Omega, i, D, \mu_\alpha^G, \mu_\delta^G)$ are the 11 model parameters, and $\boldsymbol{y}$ are the observations outlined in Section 2.2. Since the *Gaia*, *Hipparcos*, and ALMA observations are statistically

independent, we can split the likelihood into

$$\begin{aligned} P(\boldsymbol{y} \mid \boldsymbol{\theta}) =& P(\boldsymbol{y}_{\mathrm{C6,M_1}}|\boldsymbol{\theta}) \cdot P(\boldsymbol{y}_{\mathrm{C6,M_2}}|\boldsymbol{\theta}) \cdot P(\boldsymbol{y}_{\mathrm{C10,M_1}}|\boldsymbol{\theta}) \cdot P(\boldsymbol{y}_{\mathrm{C10,M_2}}|\boldsymbol{\theta}) \cdot \\ & P(\boldsymbol{y}_{\mathit{Gaia},\mathrm{M_1}}|\boldsymbol{\theta}) \cdot P(\boldsymbol{y}_{\mathrm{Hip,M_1}}|\boldsymbol{\theta}) \end{aligned} \tag{4}$$

where we abbreviated $\boldsymbol{y}_{\mathrm{C}n,M_i} = (\alpha_{\mathrm{C}n,M_i}, \delta_{\mathrm{C}n,M_i})$ and $\boldsymbol{y}_{\mathit{Gaia}/\mathrm{Hip,M_1}} = (\alpha_{\mathrm{M_1}}, \delta_{\mathrm{M_1}}, \varpi, \mu_{\alpha^*_1}, \mu_{\delta_1})_{\mathit{Gaia}/\mathrm{Hip}}$. $\boldsymbol{y}_{\mathrm{C}n,M_i}$ and $\boldsymbol{y}_{\mathit{Gaia}/\mathrm{Hip,M_1}}$ are given in Section 2.2. Each of the likelihoods was chosen to be a Gaussian:

$$\begin{aligned} P(\boldsymbol{y}_X|\boldsymbol{\theta}) &= \mathcal{N}(\boldsymbol{m}(\boldsymbol{\theta}), \boldsymbol{\Sigma}_X) \\ &= \frac{1}{\sqrt{(2\pi)^k |\boldsymbol{\Sigma}_X|}} \exp\left(-\frac{1}{2}\left(y_X - \boldsymbol{m}(\boldsymbol{\theta})\right)^t \boldsymbol{\Sigma}_X^{-1}\left(y_X - \boldsymbol{m}(\boldsymbol{\theta})\right)\right) \end{aligned} \tag{5}$$

where $\boldsymbol{m}(\boldsymbol{\theta}) = \mathrm{E}[\boldsymbol{y}_X]$. In the case of $P(\boldsymbol{y}_{\mathit{Gaia},\mathrm{M_1}}|\boldsymbol{\theta})$ and $P(\boldsymbol{y}_{\mathrm{Hip,M_1}}|\boldsymbol{\theta})$, the non-diagonal covariance matrices Σ_{Hip} and Σ_{Gaia} are given by Expr. (1) and (2). In all other cases, the covariance matrices are diagonal with the square of the standard errors given in Section 2.2 on the diagonal.

In each case the components of the expected value $\boldsymbol{m} = E[\boldsymbol{y}_X]$ related to the sky coordinates (α, δ) of M_1 or M_2 are computed using the following model:

$$\begin{pmatrix} E[\alpha] \\ E[\delta] \end{pmatrix} = \begin{pmatrix} \alpha^0_G \\ \delta^0_G \end{pmatrix} + \begin{pmatrix} \mu^G_\alpha \\ \mu^G_\delta \end{pmatrix}(t - t_{C6}) + \begin{pmatrix} \Delta\alpha \\ \Delta\delta \end{pmatrix}. \tag{6}$$

Here, (α^0_G, δ^0_G) denote the ICRS coordinates of the binary system's centre of mass at $t = t_{C6}$:

$$\alpha^0_G \equiv \frac{m_1\ \alpha_{C6,M_1} + m_2\ \alpha_{C6,M_2}}{m_1 + m_2} - \Delta^p_\alpha \tag{7}$$

$$\delta^0_G \equiv \frac{m_1\ \delta_{C6,M_1} + m_2\ \delta_{C6,M_2}}{m_1 + m_2} - \Delta^p_\delta\,. \tag{8}$$

where the terms Δ^p_α and Δ^p_δ represent corrections for the parallax motion, accounting for the fact that $(\alpha_{C6,M_1}, \delta_{C6,M_1})$ and $(\alpha_{C6,M_2}, \delta_{C6,M_2})$ are the observed ALMA astrometric positions. The second term in Eq. (6) reflects the proper motion of the barycentre and the third term the change in coordinates with respect to the barycentre due to the orbital motion of the stars, and is computed as outlined in Supplementary Sect. 2.1.1.

We assumed no a priori correlations between the model parameters, and decomposed the prior $P(\boldsymbol{\theta})$ into:

$$P(\boldsymbol{\theta}) = \prod_{n=1}^{9} P(\theta_n) \tag{9}$$

where we implemented the following priors for each of the 11 model parameters:

$$P(m_1) = \mathcal{U}(0.6, 3.5) \quad [M_\odot] \tag{P1}$$

$$P(q) = \mathcal{U}(0.2, 5.0) \quad [\,] \tag{P2}$$

$$P(a) = \mathcal{U}(2, 15) \quad [\mathrm{au}] \tag{P3}$$

$$P(e) = \mathcal{U}(0, 0.95) \quad [\,] \tag{P4}$$

$$P(T_0) = \mathcal{U}(2009, 2030) \quad [\mathrm{yr}] \tag{P5}$$

$$P(\omega) = \mathcal{U}(0, 360) \quad [^\circ] \tag{P6}$$

$$P(\Omega) = \mathcal{U}(0, 360) \quad [^\circ] \tag{P7}$$

$$P(i) = \mathcal{U}(0, 360) \quad [^\circ] \tag{P8}$$

$$P(D) = \mathrm{Gamma}(k = 3, L = 500) \quad [\mathrm{pc}] \tag{P9}$$

$$P(\mu_\alpha^G) = \mathcal{U}(42, 46) \quad [\mathrm{mas\ yr}^{-1}] \tag{P10}$$

$$P(\mu_\delta^G) = \mathcal{U}(-20, -17) \quad [\mathrm{mas\ yr}^{-1}] \tag{P11}$$

where $\mathcal{U}(u_1, u_2)$ indicates a uniform prior between ranges u_1 and u_2. We initially explored a broader prior range for T_0 (1900–2200 yr), but all runs consistently converged to orbital periods around 11 yr. Based on this, we refined the prior to the range 2009–2030 yr.

The Gamma prior for the distance D of the system, with shape parameter $k = 3$ and scale parameters $L = 500$ pc, reflects an exponentially decreasing stellar volume density in the nearby Milky Way [55]. I.e. the prior for the distance is determined as

$$F^{-1}(p, k = 3, L = 500) \tag{10}$$

where p is a uniform random variable ($p \in [0, 1]$) and

$$F(x, k, L) = \frac{1}{\Gamma(k)} \int_0^x \frac{t^{k-1} e^{-t/L}}{L^3}\, dt\,, \tag{11}$$

with $\Gamma(k) = (k-1)!\,.$

To sample the posterior distribution, we used different sampling methods, for which nested sampling works the most efficient. More details on the sampling methods and the `ultranest` package can be found in Supplementary Sect. 2.3.1.

2.5. Inferred orbital parameters for the π^1 Gru system

Using the observational data outlined in Sect. 2.2 and the `ultranest` [56] Bayesian modeling framework, we inferred the six orbital elements, the primary mass (m_1), the mass ratio (q), the distance (D), and the proper motion of the barycentre ($\boldsymbol{\mu}^G$). To assess robustness, `ultranest` was

executed 10 times, as detailed in Supplementary Sect. 2.3.2, with a summary of results presented in Supplementary Table 8. In this section the results of the best run are presented.

The outcomes of Bayesian inference are characterized by two key metrics. First, we report the mean and standard deviation of the retrieved parameters, derived from the posterior samples (upper part of the table). The mean is weighted by the likelihood of each sample, while the standard deviation reflects the posterior spread. Second, we present the best-fit values, corresponding to the maximum posterior probability for each parameter (lower part of the table).

The run that achieved the highest maximum marginalized likelihood, and we refer to this as the `eccentric` model. The Bayesian retrieval yields $m_1 = 1.02 \pm 0.20\,\mathrm{M}_\odot$, $q = 1.04 \pm 0.05$, $a = 6.60 \pm 0.41$ au, $e = 0.023 \pm 0.017$, $T_0 = 2026.75 \pm 3.16$ yr, $\omega = 101 \pm 98°$, $\Omega = 94 \pm 23°$, $i = 14 \pm 8°$, $D = 174 \pm 9$ pc, $\mu_\alpha^G = 45.212 \pm 0.168$ mas yr^{-1}, and $\mu_\delta^G = -18.773 \pm 0.068$ mas yr^{-1}. The small eccentricity implies ω and T_0 are poorly constrained (see also Supplementary Sect. 2.3.2).

However, the Bayesian marginalized likelihood ($\log z$) – factoring in both fit quality and model complexity – indicates a preference for a circular orbit ($e = 0$) over the above eccentric model (see Supplementary Sect. 2.3.2). For a circular orbit, ω and T_0 are undefined; instead, we define T_0 as the time when the body crosses the ascending node. Similar to the eccentric case, `ultranest` was executed 10 times (see Supplementary Table 9). The highest maximum likelihood run, and we refer to this as the `circular` model. The inferred parameters are $m_1 = 1.12 \pm 0.25\,\mathrm{M}_\odot$, $q = 1.05 \pm 0.05$, $a = 6.81 \pm 0.49$ au, $T_0 = 2016.39 \pm 1.18$ yr, $\Omega = 101 \pm 36°$, $i = 11 \pm 7°$, $D = 180 \pm 10$ pc (or equivalently, $\varpi = 5.555 \pm 0.309$ mas), $\mu_\alpha^G = 45.203 \pm 0.144$ mas yr^{-1}, and $\mu_\delta^G = -18.776 \pm 0.061$ mas yr^{-1}. These results are shown in a corner plot (Extended Data Fig. 2) and summarized in Supplementary Table 6. The best-fit values are given in Supplementary Table 7.

The fit of the astrometric positions and tangential velocities to the observational data, based on these best-fit parameters, is depicted in Fig. 1. The orbital system of π^1 Gru, using the retrieved best-fit parameters, is visualized in Extended Data Fig. 3 for two different viewing angles. We deduce that the companion moves in a circular, anti-clockwise orbit relative to the AGB star, a conclusion further reinforced by ALMA and SPHERE-ZIMPOL data presented in ref. [25,26,46,57]. The arcs observed in these datasets, interpreted as segments of an anti-clockwise spiral, exhibit shapes consistent with this orbital motion. The ALMA data [25,26,57] trace the gas motion, while the SPHERE-ZIMPOL data [46], taken almost at the same time as the ALMA C6 observations, reveal that the dust tail, formed in the companion's wake, also exhibits a shape consistent with this anti-clockwise orbit.

The corner plot (Extended Data Fig. 2) demonstrates high-quality sampling with well-defined boundaries and Gaussian-like posterior distributions for m_1, q, a, D, and $\boldsymbol{\mu}^G$, underscoring the effectiveness of the `ultranest` sampling method. It also reveals the expected strong correlations between m_1, a, and D and Ω and T_0. In particular, there is a perfect positive correlation between Ω and T_0. Additionally, a strong positive degeneracy exists between a and m_1 (with linear correlation

coefficient, ρ, of 0.99), between D and a ($\rho = 0.94$) and D and m_1 ($\rho = 0.90$).

For the derived best-fit circular system parameters, the predicted tangential velocity of the barycentre, $v^G_{\rm tan}$, is 29.86 km s^{-1} with a position angle of $120.84°$. The tangential velocity anomaly, $\Delta v_{\rm tan}$, and its corresponding position angle, θ, at the *Gaia* and *Hipparcos* epochs are 7.03 km s^{-1} and $359.04°$, and 6.80 km s^{-1} and $336.39°$, respectively.

The corresponding orbital period is 11.76 ± 1.85 years. Whether this period can be linked to a long secondary period (LSP) remains unclear. The periodogram derived from the ASAS light curve of π^1 Gru reproduces the AGB pulsation period of 195.5 days well (see Sect. 4), and there are tentative indications of an LSP of approximately 10 years. However, the data span of ~ 9 years is insufficient for a detection at the $\geq 3\sigma$ level. Furthermore, given the low inclination we derive for the system, the probability of detecting an LSP is inherently low.

The relative motion fit of M_2 with respect to M_1 for the ALMA 2019 C6 and ALMA 2023 C10 data is presented in Supplementary Fig. 5. Accounting for both $\sigma_{\rm pos,abs}$ and $\sigma_{\rm pos,rel}$, the uncertainties in the relative position of M_2 with respect to M_1 in ($\alpha_\star$, δ) are (3.34, 2.09) mas for the ALMA C6 epoch and (2.92, 2.40) mas for the ALMA C10 epoch. The difference between the observed and predicted astrometric positions is (0.48, 1.60) mas at ALMA C6 and (-0.95, -1.77) mas at ALMA C10, indicating consistency within the measurement uncertainties.

The astrometric position of M_2 at the ALMA C6 epoch corresponds to an orbital contribution to the radial velocity of 0.06 km s^{-1} for the ALMA C6 epoch and 3.37 km s^{-1} for the ALMA C10 epoch (see Supplementary Sect. 2.4). This orbital motion represents only one component of the overall velocity vector field. As discussed in Sect. 3, the velocity amplitude and direction exhibit significant variation at and around the position of M_2, due to the formation of a bow shock spiral and an accretion disk. This complexity in the velocity vector field is also evident in the ALMA C6 and C10 data, particularly in the analysis of the SiO maser lines; see Sect. 2.5.1.

A comprehensive sensitivity analysis of the orbital parameter retrieval is presented in Supplementary Sect. 2.3.2. There, we systematically explore the robustness of the inferred orbital parameters by varying input assumptions, priors, and data subsets. This includes repeated runs of the Bayesian inference, alternative prior choices (e.g., for the primary mass), and exclusion of specific observational constraints. The resulting posterior distributions and best-fit values are compared to assess the stability of the solution and to identify any potential degeneracies or biases.

2.5.1 Distinguishing between (ω, Ω) and its antipodal nodes using radial velocity measurements

Although the radial velocity of π^1 Gru's barycentre remains unknown, we can use the difference in the orbital contribution to the radial velocity of M_1 at the ALMA C6 and ALMA C10 epochs to initially resolve the (ω, Ω) versus $(\omega + 180°, \Omega + 180°)$ ambiguity.

For the specific `circular` configuration, the predicted orbital contribution to the radial velocity of M_1 is approximately 0.21 km s^{-1} at the ALMA C6 epoch, and about -1.67 km s^{-1} at the ALMA C10 epoch (see Supplementary Fig. 6). This leads to a predicted change in radial velocity between both epochs of $\Delta v_{\rm rad}^{\rm orb} \approx -1.9$ km s^{-1}.

This preliminary prediction can be compared to observational constraints. Specifically, we use the central velocities of various molecular lines to estimate $v'_{\rm rad}$ of M_1 in the kinematic local standard of rest (LSRK) frame at both the ALMA C6 and ALMA C10 epochs (see Supplementary Eq. (108)). To achieve this, we extracted data from a small aperture (of diameter $0\farcs04$) centered on the AGB continuum peak and select high-excitation lines probing the inner few stellar radii around the AGB star (see Supplementary Fig. 7). We used the extended configuration ALMA C6 2019 data with an angular resolution of $\sim 0\farcs019$ [48]. The central velocities are derived by fitting a Gaussian to the line profiles.

From this analysis, we obtain an LSRK velocity for M_1 of approximately -16.8 ± 1.0 km s^{-1} at the ALMA C6 epoch and -18.3 ± 0.5 km s^{-1} at the ALMA C10 epoch, with corresponding spectral resolution being 1.3 km s^{-1} and 0.17 km s^{-1}, respectively. We note that the emission from behind the star is obscured and that within the inner few stellar radii, the wind could be in infall, causing the apparent velocity to be slightly blue-shifted. However, since the line profiles are fairly symmetric with aligned peaks at each epoch, this suggests that the blue-shifted bias is of similar strength at both epochs, effectively canceling out when calculating the velocity difference. The observed velocity difference is $\Delta v_{\rm rad}^{\rm orb} \approx -1.5 \pm 1.1$. The good agreement between the predicted value and the observational constraint, both of which fall within the same ballpark, is reassuring and provides an initial indication that the current combination of (ω, Ω) is likely the correct one.

This analysis also offers a first estimate of the radial velocity of π^1 Gru's barycentre, which we determine to be -14.8 ± 1.0 km s^{-1}. This yields predicted radial velocities for M_1 in the ICRS frame of -14.59 ± 1.0 km s^{-1} and -16.48 ± 1.0 km s^{-1} at the ALMA C6 and ALMA C10 epochs, respectively. When transformed into the LSRK frame, these values become -16.63 ± 1.0 km s^{-1} and -18.52 ± 1.0 km s^{-1}, which are very close to the observed LSRK velocities of -16.8 ± 1.0 km s^{-1} at the ALMA C6 epoch and -18.3 ± 0.5 km s^{-1} at the ALMA C10 epoch, listed above. This predicted radial velocity for the barycentre is also confirmed when comparing to the ALMA 2023 C10 moment-1 (intensity-weighted mean velocity) map of the ^{29}SiO v=0 J=8-7 emission (panel (b) of Supplementary Fig. 8). Future ALMA line observations would provide additional velocity information, thus introducing even more observational constraints in the Bayesian fitting process.

Another validation for the current combination of (ω, Ω) comes from the 2019 ALMA C6 SiO maser data presented by Ref. [25]. We complement this with a similar analysis of the ^{28}SiO v=0, 1, 2 J=8-7 lines (panel a of Supplementary Fig. 8), and the ^{12}CO v=1 J=3-2 and ^{29}SiO v=0 J=8-7 position-velocity (PV) diagrams from the 2023 ALMA C10 data (Supplementary Fig. 8, panels d-e). Panel (c) of Supplementary Fig. 8 depicts a ^{28}SiO v=1 J=6-5 PV diagram from the 2019 ALMA C6 data. The ALMA C10 data have a higher spectral resolution and spectral line signal-to-noise

ratio (SNR) than the C6 data, allowing for a more detailed view of the velocity structure around the primary and companion stars.

In particular, high resolution SiO data reveal the velocity structure close to M_2 at both epochs. This is seen in Supplementary Fig. 8 and also in Fig. 11–12 of Ref. [25]. SiO $v > 0$ emission, mostly masers, comes from high-energy level states and thus is confined close to the star. The $v = 0$ emission shows some signs of masing and, by selecting observations at the highest angular resolutions, the region around M_1 and M_2 can be resolved whilst large-scale thermal emission is resolved-out. However, when including short baselines sensitive to extended flux, such as the 2019 combined data, $v = 0$ thermal emission on larger scales dominates, showing the circumbinary disc but obscuring the $M_1 - M_2$ interaction. Consequently, the 2019 SiO moment-1 map (intensity-weighted mean velocity) presented by Ref. [25] appears near zero at the position of M_2. However, as we discuss below, this should not – and does not – imply that the radial velocity is actually zero at that location. Instead, this is likely due to weaker SiO emission, possibly caused by partial obscuration by the companion star and its accretion disk.

In 2019, the SiO maser flow from M_1 towards M_2 showed an increasingly blue-shifted trend closer to M_2. In contrast, by 2023, this maser flow had become red-shifted; see panel (a) of Supplementary Fig. 8. Accounting for the ALMA C10 barycentric radial velocity of approximately -18.3 km s^{-1}, the relative radial velocity at and around the location of M_2 is non-zero, reflecting the radial projection of the complex velocity structure, also seen in the hydrodynamical simulations presented in Sect. 3, where the radially outflowing wind and the spiral bow shock play key roles.

The same velocity gradient is observed in the 2023 C10 ^{12}CO v=1 J=3-2 data (see panel (e) of Supplementary Fig. 8), where the radial velocity ranges from approximately -19 km s^{-1} to -12 km s^{-1} midway between M_1 and M_2; however, the emission is too weak to measure the velocity structure directly at M_2. Additionally, the CO v=1 J=3-2 emission near M_1 appears weaker, likely due to partial obscuration by the star. In this respect, the 2023 ^{29}SiO v=0 J=8-7 strong emission provides better diagnostics, with panel (d) of Supplementary Fig. 8 clearly showing the increasingly red-shifted stream towards M_2.

This streamer was progressively more blue-shifted in the 2019 data, as confirmed by the SiO maser analysis presented by Ref. [25]. The blue-shift is also evident in, for example, the ^{28}SiO v=1 J=6-5 PV diagram presented in panel (c) of Supplementary Fig. 8. This shift from a blue-shifted (2019) to a red-shifted (2023) streamer between M_1 and M_2 is consistent with the retrieved orbital configuration, including (ω, Ω), as listed in Supplementary Table 6 and shown in Extended Data Fig. 3.

3. Hydrodynamical modelling

For a circular orbit with synchronous stars, the Roche lobe radius of a star in a binary system depends solely on the system's semi-major axis and mass ratio. It is expressed as [58]:

$$R_{L,1} = \frac{0.49q^{2/3}}{0.6q^{2/3} + \log(1 + q^{1/3})} a \,, \tag{12}$$

where $R_{L,1}$ represents the radius of a sphere with a volume equivalent to that of the Roche lobe. Using the derived values for a and q, we calculate a Roche lobe radius of approximately ~ 2.61 au. For π^1 Gru A, which has a radius of ~ 1.65 au (see Sect. 4.1), this indicates that the star does not fill its Roche lobe.

Mass-loss still occurs for the AGB star due to their dust-driven winds. This material can be attracted by the companion and will be accreted. In the most simple case where the wind velocity is much larger then the orbital velocity of the companion this mechanism can be described by the classical Bondi-Hoyle-Lyttleton (BHL) [59,60] formalism. In the case of the π^1 Gru system, the orbital velocity of the companion of $\sim$16 km s^{-1} almost equals the radial expanding wind velocity of $\sim$14 km s^{-1} (as derived by Ref. [57]). This implies that a wind accretion scenario relying on this BHL formalism is not valid.

This suggests that the wind-RLOF regime, first studied in the context of symbiotic binaries by Ref. [31], offers a more promising framework to understand the structure in the circumstellar envelope of π^1 Gru A and the wind-companion interaction. For this mechanism to be effective, the dust condensation radius must extend beyond the Roche lobe, which is a reasonable assumption given that dust condensation in such environments typically occurs at a few stellar radii.

The gravitational influence of a binary companion affects the wind morphology of an AGB star in two distinct ways [61]. On the one hand, the companion's gravity focuses a fraction of the wind material towards the equatorial plane into a detached bow shock or accretion wake flowing behind the companion [62]. On the other hand, it induces an orbital motion of both stars around the barycentre. This generates a spiral shock with a stand-off radius defined by the orbital and wind velocity. The arc pattern due to the reflex motion of the mass-losing AGB star nearly reaches the orbital axis and introduces an oblate-shaped flattening of the circumstellar envelope density.

To predict the wind morphology, estimate the mass accretion rate onto the companion, and explore the nature and properties of the accretion disk expected to form around the companion star, we perform high-resolution, three-dimensional smoothed particle hydrodynamics (SPH) simulations using the PHANTOM code [63]. The numerical setup of the simulations is the same as described in Ref. [33]. The stars are modelled as sink particles that can accrete wind particles and gain their mass and momentum [33,63]. The stellar wind is modelled using the free-wind approximation, where the gravitational force of the AGB star is artificially balanced by the radiation force. This allows for a computationally simple way to launch a wind, but it does not adequately take into account

pulsations, dust formation and the impact of radiative transfer. Better wind prescriptions that incorporate pulsations [6], dust nucleation [32] or radiation transport [64] are currently under development, but a fully integrated model that combines all these effects remains to be achieved.

To model the accretion around the companion, we include H I cooling and assume the wind is atomic, with a mean molecular weight of 1.26 u [33]. The model parameters are as follows: the companion's accretion radius is $R_{2,\mathrm{accr}} = 2.15\,R_\odot$, optimized for resolving the accretion disk in the model; the stellar masses are $m_1 = 1.12\,M_\odot$ and $m_2 = 1.17\,M_\odot$; the semi-major axis is $a = 6.81\,\mathrm{au}$; and the orbital eccentricity is $e = 0.0$. The AGB star's mass-loss rate is $8 \times 10^{-7}\,\mathrm{M_\odot\,yr^{-1}}$ [57], and the initial wind velocity is $8.85\,\mathrm{km\,s^{-1}}$ at the stellar surface, corresponding to a terminal velocity of $\sim 18\,\mathrm{km\,s^{-1}}$. To optimize computational efficiency, particles beyond a radius of $30\,\mathrm{au}$ are removed from the simulation. The simulation spans approximately 14.5 orbital periods, at which point the accretion disk's mass stabilizes, indicating equilibrium between the wind accretion rate onto the disk and the mass accretion rate from the disk onto the companion. The simulation employs roughly 500,000 particles with a particle mass of $3.05 \times 10^{-11}\mathrm{M_\odot}$.

The resulting density distribution around the stars is presented in Extended Data Fig. 4. A bow shock spiral originates in front of a dense accretion disk that surrounds the companion. The zoomed-in figure (panel b) reveals the 3D shape of the accretion disk, that is roughly circular in the orbital plane and flaring in the edge-on view, and reveals the tangential motion of matter in the accretion disk around the companion. Material is orbiting with tangential velocities in the range $[0.8, 1.0]$ times the Keplerian velocity, i.e. $(0.8 - 1.0) \times \sqrt{Gm_2/r}$.

Adopting the method described in Ref. [33], we estimate that the disk has a radius of $r_{\mathrm{disk}} = 0.83\,\mathrm{au}$, a mass of $M_{\mathrm{disk}} = 2.0 \times 10^{-6}\,\mathrm{M_\odot}$, a flared edge-on profile with maximum scale height $H(r_{\mathrm{disk}}) = 0.144\,\mathrm{au}$, and a maximum midplane density at $r = 0.09$ au of $\rho_{\mathrm{max}} = 8 \times 10^{-11}\,\mathrm{g\,cm^{-3}}$. The estimated mass accretion efficiency onto the companion sink particle is 14.5%, corresponding to a mass accretion rate of $1.16 \times 10^{-7}\,\mathrm{M_\odot\,yr^{-1}}$. Given that the outer disk radius is less than 70% of the companion's Roche lobe radius (of ∼1.6 au), tidal interactions that could truncate the disk can be safely neglected.

4. Stellar evolution

In order to access the evolutionary state of π^1 Gru A, and estimate its initial mass, stellar properties are derived like the luminosity, temperature, and radius as well as its pulsation period. These properties are then compared to stellar evolution models to infer the star's evolutionary state and initial mass.

4.1. Stellar properties of π^1 Gru A

To estimate the luminosity and temperature of π^1 Gru A, we rely on the $(V-K)$ colour index, which is a well-established temperature indicator for late-type stars. The mean Johnson V-band magnitude is reported in the ASAS-SN catalogue of variable stars as $V = 7.06$ with amplitude of variation of 1.48[65]. The K-band amplitude of variation is far less, ∼0.1, and we here use $V - K = 8.61$ as reported by Ref. [66].

To estimate both interstellar and circumstellar extinction along the line of sight, we use the $E(BP-RP)$ colour excess from the *Gaia* DR3 archive [54]. The *Gaia* BP band covers wavelengths from approximately 400 to 500 nm, while the RP band spans 600 to 750 nm. According to *Gaia* DR3, the colour excess is listed as $E(BP - RP) = 1.6056$. Using established photometric transformations between *Gaia* and other systems (https://gea.esac.esa.int/archive/documentation/GEDR3/Data_processing/chap_cu5pho/cu5pho_sec_photSystem/cu5pho_ssec_photRelations.html), we derive a corresponding *Hipparcos* $E(B-V)$ value of 1.40.

The total reddening caused by dust depends on the ratio of total to selective extinction, $R_V = A_V/E(B-V)$. For the diffuse interstellar medium, $R_V \sim 3.1$, but in dense or dusty environments, such as circumstellar regions of AGB stars, grain growth leads to higher R_V values. Typical values range between 3.5 and 4.5 [67]. For oxygen-rich red supergiant stars, which share their dust composition with oxygen-rich AGB stars, R_V has been determined to be ~ 4.2 [68]. Applying this value, we calculate $A_V = 5.87 \pm 0.70$. Using the extinction relations from Ref. [69], we determine that $(V-K)_0 = 4.55 \pm 1.65$.

To compute the bolometric correction, BC_K, we use the $((V-K)_0, BC_K)$ relation from Ref. [70], which yields $BC_K = 2.78 \pm 0.27$. Adopting the solar bolometric magnitude of $M_{\mathrm{bol},\odot} = 4.74$ and a best-fit distance of 169.38 pc from the eccentric model, we derive a luminosity of 7,300±2,100 $L_\odot$. At a distance of 180 pc, the luminosity increases by ∼1,000 $L_\odot$.

The angular diameter of π^1 Gru A, measured at 1.65 μm, is 18.37 ± 0.18 mas [71]. At a distance of 169.38 pc, this translates to a stellar radius of $334 \pm 20\ R_\odot$. Using the derived luminosity, radius and mass (of $1.12 \pm 0.25\ M_\odot$), the effective temperature is determined to be 2,900±200 K with surface gravity of $\log_{10} g$ [cgs] = -0.56 ± 0.11, or $\log_{10} g$ [cgs] = -0.51 ± 0.10 in the case of the higher current mass m_1 derived from the Gaussian prior sensitivity study.

4.2. Initial mass of π^1 Gru A

We provide an independent estimate of the initial mass from analysing π^1 Gru A's variability, when coupled with stellar evolution models. The stellar evolution models help to constrain the nature and evolution of π^1 Gru A along the AGB phase.

We construct a core-mass luminosity diagram using AGB models between $1\,M_\odot$ and $2\,M_\odot$ with solar metallicity, using models from Ref. [35], which is shown in Supplementary Fig. 10. The luminosity of π^1 Gru A is indicated by the dashed lines, along with upper and lower bounds from the literature. This diagram illustrates that models with initial masses of around $1.7\,M_\odot$ are the best fit to the luminosity as explained below, but the uncertainties are large. This figure demonstrates the degeneracy in the core-mass luminosity relationship for low-mass AGB stars. However, models below $1.25\,M_\odot$ can be ruled out owing to the fact that these do not experience any third dredge-up mixing [35] which is needed to explain the fact that π^1 Gru A is an intrinsic S-type AGB star with a clear detection of the radioactive isotope of s-process element technetium (^{99}Tc) [72]. Third dredge-up causes the star's surface C/O ratio to increase from its RGB value of ≈ 0.3 to ≥ 0.5, which is the minimum C/O ratio in S-type stars like π^1 Gru A. It is also possible to rule out higher-mass models such as the $2\,M_\odot$ where the predicted luminosity is higher than π^1 Gru A, especially near the end of its TP-AGB phase. Furthermore, this model becomes C-rich where the surface C/O ratio ≥ 1, higher than observed in π^1 Gru A (~ 0.97 [73]).

The Monash stellar evolution code was used to calculate the AGB models shown in Supplementary Fig. 10 and we refer to Ref. [35] for details of the input physics. We use the Mixing-length Theory of convection, with a mixing-length parameter $\alpha_{\rm MLT} = 1.86$, and assume that mixing is instantaneous in convective regions. No overshoot or convective boundary mixing is included in the calculations prior to the AGB. We set the initial metallicity to be solar, here defined to be $Z = Z_{\rm sun} = 0.014$ given that π^1 Gru A is a close AGB star found in the thin disk of the Milky Way. The evolution of the $1.7\,M_\odot$ model provides the closest match to π^1 Gru A's luminosity, although it does so only during the last few thermal pulses. This is consistent with the fact that π^1 Gru A has undergone mass loss.

A major uncertainty in AGB stellar models is calculating the third dredge-up, which depends on the numerical model for convection and the treatment of convective borders [74]. In the Monash models we include a simple prescription for convective overshoot discussed in Ref. [75], where we extend the base of the envelope by $N_{\rm ov}$ pressure scale heights during dredge-up. In order for the masses considered here to become S-type, we use $N_{\rm ov} \leq 3$. In the $1.7\,M_\odot$ model shown in Supplementary Fig. 10 we use $N_{\rm ov} = 2.5$, which results in a final C/O = 1.16 after 18 thermal pulses noting that the star only becomes C-rich at the very last thermal pulse. The total TP-AGB lifetime is $\sim$1.65 million years. Mass loss on the AGB is another major uncertainty in AGB models; see for example Ref. [74]. Using the mass-loss rate from Ref. [76] on the AGB in the $1.7\,M_\odot$ model with all the other input parameters the same results in a final C/O = 0.95, after 18 thermal pulses and a total TP-AGB lifetime of $\sim$1.7 million years.

As an additional constraint for the initial mass of π^1 Gru A, we analyse the characteristics of its pulsation. As mentioned previously, π^1 Gru A is a long period variable (LPV) star of type SRb, with a pulsation period of roughly 195.5 days. This period is listed on The International Variable Star Index (VSX) [77] and is based on combined V-band light curves from the All Sky Automated Survey [78] and Ref. [36], as well as being further substantiated by long term light curves from the American Association of Variable Star Observers (AAVSO) (https://www.aavso.org)

and the All Sky Automated Survey for Supernovae (ASAS-SN) [79]. The additional period listed in VSX of 128 d may be a result of convolution with the observing window and the true peak in the periodogram ((1/195.5 d + 1/365.25 d)$^{-1}$ $\sim$ 128 d), so we omit this from our analysis. We then assign a pulsation mode for this period by π^1 Gru A's position on the period-luminosity (PL) diagram. LPVs form multiple parallel sequences on the PL diagram, each being associated to low order radial pulsation modes with mode order descending from left to right [80], excluding the lower right sequence D which is associated with long secondary periods. In Extended Data Fig. 5 we compare π^1 Gru A with the period-luminosity diagram for the Optical Gravitational Lensing Experiment (OGLE) catalogue of LPVs for the Large Magellanic Cloud (LMC) [81], as well as the ASAS-SN catalogue of LPVs [82]. We construct the PL diagrams with J- and K_s-band photometry from 2MASS, using the NIR Wesenheit function $W_{K_s,J-K_s} = K_s - 0.686 \cdot (J - K_s)$ to calculate a reddening free magnitude. We use a distance modulus of $\mu = 18.49$ (D = 49.97 kpc) for the LMC [83], and the Bayesian geometric distances using *Gaia* DR3 parallaxes from Ref. [84] for the ASAS-SN catalogue to calculate absolute magnitudes. Additionally, we plot the PL sequence boundaries for the LMC from Ref. [85] to illustrate the positions of the sequences in the ASAS-SN PL diagram. We use the distance of 180 ± 10 pc for π^1 Gru A, which places it on sequence C' on the PL diagram. In a similar fashion to Ref. [85], we can assign the pulsation mode of the 195.5 d period to be the radial first overtone mode. However, the universality of the period-luminosity relation for LPVs remains somewhat uncertain for different metallicity environments [86,87], though the clear offset in sequence C' for the ASAS-SN PL diagram may be attributed to uncertain parallax distances for the brightest, more evolved AGB stars [88] or from saturation of the NIR photometry. Though the exact effects of metallicity on the LPV PL sequences are still under investigation, Ref. [85] compare LPVs the LMC and SMC to find that the variability amplitudes may be affected by metallicity, due to lower metallicities favouring the production of C-rich stars which have higher variability amplitudes and periods than O-rich stars on average. More recently, Ref. [87] find that stability against pulsation is likely sensitive to chemical composition, though further investigation is required to better understand the effects on LPVs in general. We have included the PL diagrams from OGLE (LMC) and ASAS-SN (all-sky) to represent different metallicity environments, and that the pulsation mode appears to be consistent. Ultimately, the present mode assignment is thus made under the assumption that the metallicity environment does not significantly shift the PL sequences, or their slopes, such that at the very least the period can be reasonably assigned to a sequence and thus a pulsation mode.

Once we have assigned a pulsation mode to the period, we make comparisons to results from stellar evolution codes. We estimate the pulsation characteristics for the TP-AGB with the results of the linear pulsation models from Ref. [37], which provides an interpolation code to find the pulsation periods and amplitude growth rates for the radial pulsation modes given a set of stellar parameters which we take from the Monash models. In Supplementary Fig. 11, we begin by comparing π^1 Gru A to the theoretical P-L diagram for models with initial masses of $1, 1.5$ and $2\,\mathrm{M}_\odot$. These models use the same initial metallicity, mass-loss η and mixing-length α_{MLT} as above, with $N_{\mathrm{ov}} = 2.0$. The pulsation period and luminosity $(7,300\,\mathrm{L}_\odot)$ for π^1 Gru A is consistent with models between initial mass $1.5-2\,\mathrm{M}_\odot$. We also include the model tracks on the HR diagram with the luminosity and effective temperature derived above for π^1 Gru A, and find them to be roughly

consistent with the PL diagram.

As with the above discussion on the core-mass luminosity relationship, we adopt a likely mass of approximately $1.7\,\mathrm{M}_{\odot}$. Fig. 2 presents the time evolution of the total stellar mass, luminosity, pulsation periods for the first and fundamental modes, the amplitude growth rates of these modes and the C/O for this model. The amplitude growth rate describes the fractional rate of change in the radial amplitude per cycle, and may be used as a general indicator of the dominant pulsation mode, though we do note that this quantity is still subject to the uncertain interaction between convection and pulsation. The total mass of this model at the onset of the TP-AGB is $1.62\,\mathrm{M}_{\odot}$ due to mass loss on the RGB, and reaches the current mass of $\sim 1.46\,\mathrm{M}_{\odot}$ during the last two thermal pulses. The combined period and luminosity of π^1 Gru A appears to be consistent with the last few thermal pulses for this model mass. Importantly, the growth rates suggest that even in the last few thermal pulses, the first overtone mode can still be dominant at the period and luminosity of π^1 Gru A. That is, despite appearing to be late on the TP-AGB, π^1 Gru A can still appear as a semi-regular variable, instead of a Mira variable pulsating in the fundamental mode.

We also demonstrate the effects of key model parameters on this estimate, namely the convective overshoot parameter N_{ov} and the mass-loss prescription on the TP-AGB. Fig. 2 demonstrates the effect of different N_{ov}, where a lower value of $N_{\mathrm{ov}} = 2.0$ will terminate the TP-AGB with greater mass-loss in the final interpulse phases, and will only reach a C/O ratio of ~ 0.7, which is somewhat lower than the estimated value for π^1 Gru A. The previously described model with the mass-loss prescription from Ref. [76] behaves somewhat differently compared to this model, due to continuous mass-loss over the whole TP-AGB instead of episodic mass-loss in the final thermal pulses. This model approaches a total mass of $1.46\mathrm{M}_{\odot}$ before the model luminosity, pulsation period and C/O reaches the measured values, and it also survives for roughly 0.1 Myr longer. This prescription does not however take into account the episodic nature of pulsation-enhanced, dust-driven winds that π^1 Gru A is more likely experiencing. Furthermore, it must be mentioned that neither mass-loss prescription accounts for any effects a close companion may have on mass-loss rates and pulsation, a topic which requires further detailed investigation.

5. Orbital evolution

Given the current properties of the binary system, as well as the estimated initial mass of π^1 Gru C, the orbital properties are projected back in time to understand the past evolution of the system, as well as forward in time to understand the future evolution of the system. To do this, an orbital evolution model is established, which is then used to project the system properties. Finally, a sensitivity study is performed to understand the impact of the observed properties on the final outcome of the system.

Given that gravitational wave radiation and magnetic braking are negligible for the system under consideration, the change in orbital elements arises from two main components. First, mass loss – in particular during the giant phases – may lead to a widening of the companion's orbit.

Second, tidal dissipation may cause the orbit to shrink. To compute the changes in the orbital parameters, both effects must be taken into account (the change in eccentricity is computed as the change in the square of the eccentricity to prevent numerical issues when the eccentricity is close to 0):

$$\frac{1}{a}\frac{\mathrm{d}a}{\mathrm{d}t} = \frac{1}{a}\frac{\mathrm{d}a}{\mathrm{d}t}\bigg|_{\rm wind} + \frac{1}{a}\frac{\mathrm{d}a}{\mathrm{d}t}\bigg|_{\rm tides} , \quad \frac{\mathrm{d}e^2}{\mathrm{d}t} = \frac{\mathrm{d}e^2}{\mathrm{d}t}\bigg|_{\rm wind} + \frac{\mathrm{d}e^2}{\mathrm{d}t}\bigg|_{\rm tides} . \tag{13}$$

Here, the first term represents the contribution of wind mass loss, while the second term accounts for tidal dissipation.

5.1. Impact of stellar winds on orbital dynamics

If the donor star, here M_1, is losing mass and mass transfer is non-conservative, the companion star (M_2) will accrete a fraction of the material and the rest will be lost, thereby carrying away angular momentum from the system and impacting the orbital separation and eccentricity. We first consider the case of a circular orbit, and then work out the equations for an eccentric orbit.

5.1.1 The case of a circular orbit

In the case of a circular orbit, the change in orbital separation due to wind mass loss is given by [89]

$$\frac{1}{a}\frac{\mathrm{d}a}{\mathrm{d}t}\bigg|_{\rm wind} = -2\,\frac{\dot{L}_{\rm orb}}{L_{\rm orb}}\bigg|_{\rm wind} - 2\frac{\dot{m}_1}{m_1} - 2\frac{\dot{m}_2}{m_2} + \frac{\dot{m}_1+\dot{m}_2}{m_1+m_2} \tag{14}$$

$$= -2\,\frac{\dot{L}_{\rm orb}}{L_{\rm orb}}\bigg|_{\rm wind} - 2\frac{\dot{m}_1}{m_1}\left(1 - \frac{\beta}{q} - \frac{1-\beta}{2}\frac{1}{(1+q)}\right) , \tag{15}$$

where $q = m_2/m_1$, $\dot{m}_1$ is the mass loss from the primary (here taken negative) and $\dot{m}_2$ the mass gained by the companion, i.e. $\dot{m}_2 = -\beta\dot{m}_1$, with β the mass accretion efficiency. If $\beta < 1$, mass transfer is non-conservative. The change in angular momentum can be expressed as [5]

$$\dot{L}_{\rm orb}\Big|_{\rm wind} = \eta a^2 \Omega_o (\dot{m}_1 + \dot{m}_2) , \tag{16}$$

where Ω_o is the orbital frequency and η the specific orbital angular momentum of the material lost in units of the orbital angular momentum of the system per reduced mass. Combining Eqs. (15)–(16), the change in the orbital separation can be written as [5]

$$\frac{1}{a}\frac{\mathrm{d}a}{\mathrm{d}t}\bigg|_{\rm wind} = -2\frac{\dot{m}_1}{m_1}\left(1 - \frac{\beta}{q} - \eta(1-\beta)\frac{1+q}{q} - \frac{1-\beta}{2}\frac{1}{1+q}\right) . \tag{17}$$

Assuming a fast isotropic wind, where the velocity of the wind at the location of the companion is much larger than the orbital velocity, the mass accretion efficiency is given by the Bondi-

Hoyle-Lyttleton (BHL) analytical approximation [5]

$$\beta_{\rm BHL} = \frac{q^2}{(1+q)^2} \frac{v_{\rm orb}^4}{v_{\rm w}(v_{\rm w}^2 + v_{\rm orb}^2)^{3/2}} \, , \tag{18}$$

where $v_{\rm orb} = \sqrt{G(m_1+m_2)/a}$ is the orbital velocity and $v_{\rm w}$ is the wind velocity. In this specific case (in this context also called Jeans' mode), the specific angular momentum taken from the orbit and transferred to the outflowing gas is given by [5]

$$\eta_{\rm iso} = \frac{q^2}{(1+q)^2} \, . \tag{19}$$

However, in the case of AGB binary stars, the fast-wind scenario may not hold. For example, in this particular case of π^1 Gru A and C, the orbital velocity and the wind velocity at the location of the companion are both around 15 km s^{-1}. In such a case, no simple analytical expressions exist for β and η. Instead, these quantities must be computed numerically using detailed hydrodynamical simulations (see, e.g., Sect. 3). Performing such models throughout the evolution of the system is extremely computationally expensive, and infeasible with current computational resources. However, we can rely on the work of Ref. [5], who calibrated β and η as a function of the mass ratio q and the ratio of the terminal wind velocity to the orbital velocity, $v_\infty/v_{\rm orb}$, using their 3D hydrodynamical simulations. These authors obtained that:

$$\beta\left(q, \frac{v_\infty}{v_{\rm orb}}\right) = \min\left[\left(0.75 + \frac{1}{1.7 + 0.3/q + \left((0.5+0.2/q)\frac{v_\infty}{v_{\rm orb}}\right)^5}\right)\beta_{\rm BHL}, 0.3, 1.4q^2\right] \, , \tag{20}$$

$$\eta\left(q, \frac{v_\infty}{v_{\rm orb}}\right) = \min\left[\frac{1}{\max\left(1/q, 0.6q^{-1.7}\right) + \left((1.5+0.3/q)\frac{v_\infty}{v_{\rm orb}}\right)^3} + \eta_{\rm iso}, 0.6\right] \, . \tag{21}$$

As these equations depend on the terminal wind velocity, this property needs to be computed throughout the entire stellar evolution. Similar to Ref. [90], we assume the terminal wind velocity to be a fraction of the escape velocity, i.e.

$$v_\infty = \sqrt{2\alpha_W \frac{Gm_1}{R_1}} \, , \tag{22}$$

where α_W is a constant taken to be 1/8 [90].

5.1.2 The case of an eccentric orbit

When the orbit is eccentric, the change in the orbital separation and eccentricity due to mass loss becomes more complicated as it becomes phase-dependent. The change in the orbital parameters

is then given by [91]

$$\left.\frac{1}{a}\frac{\mathrm{d}a}{\mathrm{d}t}\right|_{\mathrm{wind}} = -2\frac{\dot{m}_1}{m_1}\left(1-\frac{\beta}{q}-\eta(1-\beta)\frac{1+q}{q}-\frac{1-\beta}{2}\frac{1}{1+q}\right)\left[\frac{e^2+2e\cos f+1}{1-e^2}\right] \tag{23}$$

$$\left.\frac{\mathrm{d}e^2}{\mathrm{d}t}\right|_{\mathrm{wind}} = -4\frac{\dot{m}_1}{m_1}\left(1-\frac{\beta}{q}-\eta(1-\beta)\frac{1+q}{q}-\frac{1-\beta}{2}\frac{1}{1+q}\right)\left[e^2+e\cos f\right] \ . \tag{24}$$

Integrating these equations over the true anomaly f as a function of time is computationally expensive. Instead, the change in the orbital separation and eccentricity can be computed by averaging over the orbital period, allowing these averages to be used in the orbital evolution equations. The orbit-averaged quantities can be computed using [91]

$$\langle(\ldots)\rangle = \frac{(1-e^2)^{3/2}}{2\pi}\int_0^{2\pi}(\ldots)\frac{\mathrm{d}f}{(1+e\cos f)^2} \ . \tag{25}$$

However, the dependence of β and η on the true anomaly f remains an open question, not fully understood or calibrated, therefore requiring further investigation. It can be hypothesized that the mass accretion efficiency, β, is proportional to

$$\frac{(1+e\cos f)^2}{a^2(1-e^2)^2},$$

as β_{BHL} primarily depends on the inverse square of the orbital distance (a consequence of the orbital velocity scaling as the fourth power in orbital velocity, in the limit where the orbital velocity is larger than the wind velocity). Conversely, the specific angular momentum carried away by the wind, η, can be assumed independent of the true anomaly, consistent with the assumption that η_{iso} does not vary with f. Under these assumptions, the changes in orbital separation and eccentricity due to mass loss can be expressed as:

$$\left\langle\frac{1}{a}\frac{\mathrm{d}a}{\mathrm{d}t}\right\rangle\Bigg|_{\mathrm{wind}} = -2\frac{\dot{m}_1}{m_1}\left(1-\frac{\beta_{\mathrm{enh}}}{q}-\eta(1-\beta_{\mathrm{enh}})\frac{1+q}{q}-\frac{1-\beta_{\mathrm{enh}}}{2}\frac{1}{1+q}\right) \tag{26}$$

$$\left\langle\frac{\mathrm{d}e^2}{\mathrm{d}t}\right\rangle\Bigg|_{\mathrm{wind}} = -4e^2\frac{\dot{m}_1}{m_1}\langle\beta\rangle\left(\frac{1}{q}-\eta\frac{1+q}{q}-\frac{1}{2}\frac{1}{1+q}\right) \ . \tag{27}$$

where

$$\beta_{\mathrm{enh}} = \langle\beta\rangle\frac{1+e^2}{1-e^2}$$

is the enhanced mass accretion efficiency effect for the change in the orbital separation,

$$\langle\beta\rangle = \beta_{\mathrm{c}}\frac{1}{\sqrt{1-e^2}}$$

is the average mass accretion efficiency over an orbit, and β_{c} is the mass accretion efficiency for a circular orbit (with the same a), taken from Eq. (20). These equations have been tested against a limited sample of hydrodynamic models of eccentric systems from Ref. [92], giving consistent results.

5.2. Impact of tidal dissipation on orbital dynamics

To calculate the rate of change of the orbital separation and eccentricity due to tidal interactions, the tidal potential must be calculated. Using the tidal potential, the tidal strength can be computed and the orbital evolution equations can be solved. Tidal dissipation of an evolved star is dominant compared to the dissipation during the MS for the same orbital distance [8]. Changes in the orbital evolution will therefore mainly occur during these giant phases (see Sect. 5.4). As evolved stars are known to be slow rotators [93], the rotation of the star can be neglected and only the tidal dissipation of the evolved star will be taken into account.

5.2.1 Tidal potential

For two bodies, where only the deformation of one object is considered, the tidal potential is given by the difference between the gravitational potential induced by the secondary object at each point of the extended primary body and its value at its barycentre. The tidal potential Ψ can be expressed as [94]:

$$\Psi(r,\theta,\varphi,t) = \mathrm{Re}\left\{\sum_{l=2}^{\infty}\sum_{m=0}^{l}\sum_{n=-\infty}^{\infty}\frac{Gm_2}{a}A_{l,m,n}(e,i)\left(\frac{r}{a}\right)^l \times Y_l^m(\theta,\varphi)\exp(-\mathrm{i}n\Omega_o t)\right\} , \quad (28)$$

where r, θ, φ are the spherical coordinates centered at the origin of the reference frame attached to the primary centre of mass, Y_l^m are the spherical harmonics, and $A_{l,m,n}$ are the tidal coefficients [43,94]

$$A_{l,m,n}(e, i=0) = \frac{4\pi}{2l+1}\epsilon_m\epsilon_{m,n}Y_l^m(\pi/2,0)h_n^{l,m}(e) , \quad (29)$$

with $h_n^{l,m}(e)$ the Hansen coefficients, $\epsilon_m = 1$ for $m = 0$ and $\epsilon_m = 2$ for $m > 0$, where $\epsilon_{m,n} = 1$ for $m > 0$ or $m = n = 0$, $\epsilon_{m,n} = 2$ for $m = 0$, $n > 0$ and $\epsilon_{m,n} = 0$ for $m = 0$, $n < 0$ to ensure orthogonality. For companions not too close to their host star, the quadrupolar approximation [95] is valid and only $l = 2$ needs to be taken into account, which results in $A_{2,0,n}(e) = \sqrt{\pi/5}\ h_n^{2,0}(e)$ and $A_{2,2,n}(e) = \sqrt{6\pi/5}\ h_n^{2,2}(e)$. The contribution from $m = 1$ vanishes for $i = 0$.

The Hansen coefficients are given by [43]

$$\left(\frac{a}{r'}\right)^{l+1}e^{imf} = \sum_{n=-\infty}^{\infty}h_n^{l,m}(e)\exp(-inM) , \quad (30)$$

which leads to

$$h_n^{l,m}(e) = \frac{1}{2\pi}\int_0^{2\pi}\left(\frac{a}{r}\right)^{l+1}\exp\left[i(mf - nM)\right]\,\mathrm{d}M , \quad (31)$$

with M the mean anomaly, f the true anomaly, and r the instantaneous orbital distance (see Sect. 2.1). By using Kepler's equations, the Hansen coefficients can be written as [96]

$$h_n^{l,m}(e) = \frac{(1-e^2)^{1/2-l}}{2\pi} \int_0^{2\pi} (1+e\cos f)^{l-1} \cos(mf - nM)\,\mathrm{d}f \,, \tag{32}$$

which is integrated numerically. In the special case of a circular orbit ($e = 0$), the Hansen coefficients simplify to $h_n^{l,m}(e) = \delta_n^m$. Consequently, $A_{2,0,0}(0) = \sqrt{\pi/5}$ and $A_{2,2,2}(0) = \sqrt{6\pi/5}$.

5.2.2 Tidal orbital evolution equations

The tidal orbital evolution is determined by the rate of change of the orbital energy and angular momentum, which are given by [43,94]

$$\dot{E}_{\rm orb}\Big|_{\rm tides} = -\sum_{l=2}^{\infty}\sum_{m=0}^{\infty}\sum_{n=-\infty}^{\infty} E_n^{l,m} \,, \quad \dot{L}_{\rm orb}\Big|_{\rm tides} = -\sum_{l=2}^{\infty}\sum_{m=0}^{\infty}\sum_{n=-\infty}^{\infty} L_n^{l,m} \tag{33}$$

where

$$E_n^{l,m} = n\Omega_o \mathcal{T}_n^{l,m} \,, \quad L_n^{l,m} = m\mathcal{T}_n^{l,m} \,, \tag{34}$$

$$\mathcal{T}_n^{l,m} = \frac{(2l+1)R_\star |\varphi_T(R_\star)|^2}{8\pi G} \,\mathrm{Im}(k_n^{l,m}) \,. \tag{35}$$

Here, $R_\star$ is the stellar radius, $\varphi_T(R_\star)$ the tidal potential at the stellar radius, and $k_n^{l,m}$ the Love number (see Sect. 5.2.3). $\mathcal{T}_n^{l,m}$ can be rewritten by plugging in the tidal potential as

$$\mathcal{T}_n^{l,m} = \frac{(2l+1)}{8\pi}\frac{Gm_2^2}{a}|A_{l,m,n}(e)|^2 \left(\frac{R_\star}{a}\right)^{2l+1} \mathrm{Im}(k_n^{l,m}) \,. \tag{36}$$

Having the tidal power and torque, the tidal orbital evolution can be calculated. The change in semi-major axis is given by ref. [43]

$$\frac{1}{a}\frac{\mathrm{d}a}{\mathrm{d}t}\bigg|_{\rm tides} = \frac{2a}{Gm_2m_1}\,\dot{E}_{\rm orb}\Big|_{\rm tides} \tag{37}$$

$$= -\frac{2l+1}{4\pi}\frac{m_2}{m_1}\left(\frac{R_\star}{a}\right)^{2l+1} \sum_{l=2}^{\infty}\sum_{m=0}^{\infty}\sum_{n=-\infty}^{\infty} n\Omega_o |A_{l,m,n}(e)|^2\,\mathrm{Im}(k_n^{l,m}) \tag{38}$$

$$= -\frac{5}{4\pi}\frac{m_2}{m_1}\left(\frac{R_\star}{a}\right)^{5} \sum_{m=0}^{\infty}\sum_{n=-\infty}^{\infty} n\Omega_o |A_{2,m,n}(e)|^2\,\mathrm{Im}(k_n^{2,m}) \,, \tag{39}$$

when assuming the quadrupolar approximation. The change in eccentricity is given by ref. [43]

$$\frac{\mathrm{d}e^2}{\mathrm{d}t}\bigg|_{\rm tides} = \frac{2a}{Gm_2m_1}\left((1-e^2)\,\dot{E}_{\rm orb}\Big|_{\rm tides} - \Omega_o\sqrt{1-e^2}\,\dot{L}_{\rm orb}\Big|_{\rm tides}\right) \,, \tag{40}$$

which can be rewritten in terms of the Love numbers as:

$$\left.\frac{\mathrm{d}e^2}{\mathrm{d}t}\right|_{\mathrm{tides}} = -\frac{2a}{Gm_2m_1}\sqrt{1-e^2}\Omega_o \sum_{l,m,n}\left(n\sqrt{1-e^2}-m\right)\mathcal{T}_n^{l,m} \tag{41}$$

$$= -\frac{2l+1}{4\pi}\frac{m_2}{m_1}\left(\frac{R_\star}{a}\right)^5\sqrt{1-e^2}\Omega_o \sum_{l,m,n}\left(n\sqrt{1-e^2}-m\right)|A_{l,m,n}|^2\,\mathrm{Im}(k_n^{l,m}) \tag{42}$$

$$= -\frac{5}{4\pi}\frac{m_2}{m_1}\left(\frac{R_\star}{a}\right)^5\sqrt{1-e^2}\Omega_o \sum_{m,n}\left(n\sqrt{1-e^2}-m\right)|A_{2,m,n}|^2\,\mathrm{Im}(k_n^{2,m})\,. \tag{43}$$

again using the quadrupolar approximation. Once the tidal Love numbers are known, the tidal orbital evolution can be calculated.

5.2.3 Tidal Love Numbers

The imaginary part of the Love number has two components: the equilibrium tide dissipation and the dynamical tide dissipation. The equilibrium tide dissipation originates from the turbulent friction applied by the turbulent convection on the displacement induced by the hydrostatic deformation of the body triggered by the gravitational companion of a companion [97]. The tidal Love number of the equilibrium tide for evolved stars can be calculated following Sect. 2.3.1 of Ref. [8]. The dynamical tide dissipation arises from the excitation of waves due to the gravitational potential of the companion. For evolved stars, the dynamical tide consists of the excitation and dissipation of progressive internal gravity waves [8] and can be calculated following Sect. 2.3.2 of Ref. [8]. The total tidal Love number is calculated by summing the equilibrium and dynamical tide contributions. The equations for the tidal Love numbers provided by Ref. [8] are specifically designed to calculate the tidal Love number for $l = m = n = 2$. The tidal Love number is an intrinsic property of the perturbed body, defined as the ratio of the primary's gravitational potential perturbation — induced by the companion's presence — to the tidal potential, evaluated at the surface. Since the gravitational potential perturbation follows a linear response, the dependence on the tidal potential cancels out within the equations, eliminating any dependence on m and n. As a result, only the tidal frequency ($\omega_t = n\Omega_o - m\Omega_s$, where Ω_s is the spin frequency if rotation were to be considered) varies when evaluating different combinations of m and n.

5.3. Choice of stellar structure and evolutionary models

The stellar evolutionary models from the Monash stellar evolutionary code presented in Sect. 4 do not provide the necessary output parameters needed to calculate the tidal Love numbers. Therefore, different stellar evolutionary models will be used in this section. These models are computed using the Modular Experiments in Stellar Astrophysics (MESA) code [98] with the inlist of Ref. [8] that is based on the inlist of Ref. [99] to be consistent with the Monash code. These models have initial

masses between 1 and 2 $M_\odot$ at solar metallicity ($Z = 0.0134$) and are evolved from the pre-main sequence to the white dwarf phase.

5.4. Orbital evolution of the π^1 Gru system

To compute the orbital evolution of the π^1 Gru system, we need to estimate the current stellar age of the system. To evaluate the current stellar age, we use the stellar evolutionary model to determine the time at which the mass of the primary star equals the current mass. At this moment in time, we impose the current system parameters. The orbital evolution is then integrated (using a first-order Euler method, a Runge–Kutta 4th order scheme was also tested and results in exactly the same solution. To reduce computational time, the Euler method was chosen) until the primary star reaches the white dwarf phase forward in time, as well as backward in time until the primary star reaches the PMS phase. As discussed in Supplementary Sect. 2.3.2, which addresses the sensitivity of the prior on m_1, there are two potential scenarios for the current mass of π^1 Gru A. The first scenario where π^1 Gru A starts with an initial mass of 1.7 $M_\odot$ and has a current mass of 1.23 $M_\odot$ ($q_{\text{current}} = 1.03$ $M_\odot$, $a_{\text{current}} = 7.10$ au, $e_{\text{current}} = 0$), and the second scenario where π^1 Gru A starts with an initial mass of 1.5 $M_\odot$ and has a current mass of 1.12 $M_\odot$ ($q_{\text{current}} = 1.05$ $M_\odot$, $a_{\text{current}} = 6.81$ au, $e_{\text{current}} = 0$).The orbital evolution is calculated for both scenarios. The results of this evolution are shown together with a zoom-in to the TP-AGB phase in Supplementary Fig. 9 for the first scenario and Fig. 3 for the second. For clarity on the timescale, we plot "stellar age – stellar age WD [yr]" on the x-axis, where "stellar age WD" indicates the age at which the white dwarf (WD) has cooled to a luminosity of 10^{-1} $L_\odot$. During these evolutionary calculations, we follow the evolution of the primary star, while the secondary star is assumed to be a non evolving companion (where the mass is increased by accreting material lost from the primary). This is a adequate assumption if the companion is a lower mass main-sequence star, but it is also possible that the companion is a white dwarf with a complicated history (see Supplementary Sect. 5). In this second scenario our computations are thus only valid from the moment π^1 Gru C became a white dwarf, from which point in time the mass will remain constant.

Tracing the system's past, the orbital evolution calculations indicate that the system parameters remained relatively unchanged during the MS and HB phases. During the RGB phase, the mass loss from π^1 Gru A causes the orbital separation to increase. The gradual change in orbital distance starts to change more dramatically during the AGB phase, especially during the TP-AGB phase. During this phase, the non-conservative mass loss from the system is able to lose a lot of angular momentum as it is significantly enhanced due to the comparable wind and orbital velocity (see Sect. 5.1.1). This causes the orbit to shrink instead of expand. Additionally, tidal dissipation became more significant during the AGB phase compared to the RGB phase, as the star's radius increased substantially. This leads to a continuous decrease in orbital separation throughout the TP-AGB phase, ultimately resulting in the current configuration of the system. Projecting into the future, this trend of decreasing orbital separation persists, eventually resulting in a common envelope phase. However, this assumes that stellar rotation is neglected. When rotation is taken into account, the tidal frequency decreases, leading to reduced tidal dissipation.

Throughout the evolution of this system, the equilibrium tide dissipation dominates over the dynamical tide dissipation, where the dynamical tide dissipation only contributes with a factor 10^{-5} in strength compared to the equilibrium tide dissipation. This is in line with the results of Ref. [8].

A sensitivity analysis of the orbital evolution is performed in Supplementary Sect. 4.1, where the impact of uncertainties in the system parameters on the orbital evolution is discussed, including the current semi-major axis, the current mass of π^1 Gru A, the current mass of π^1 Gru C, and the initial mass of π^1 Gru A. Within these uncertainties, the orbital evolution remains qualitatively similar, with the system evolving towards a common envelope phase.

5.5. The effect of a non-circular orbit

The Bayesian retrieval of the multi-epoch proper motion ALMA, *Gaia* and *Hipparcos* observations indicates that the current eccentricity of the system is zero. Therefore, the sensitivity study of the orbital dynamics presented in the previous section considered only circular orbits. An important question to address is how this system transitioned to a circular orbit.

To examine how rapidly the system circularizes, the current eccentricity is increased while keeping the other orbital parameters constant. The results of this analysis are shown in Extended Data Fig. 6. The figure illustrates that, in the case of a non-zero initial eccentricity, the system begins to circularize during the TP-AGB phase, but the circularization process is not rapid at the start of this phase. At the current estimated age of the system, the eccentricity is expected to retain about 80% of its initial value. For higher eccentricity cases, tidal circularization involves more wave numbers (see Sect. 5.2.2), causing the circularization process to accelerate, but it must also remove a greater amount of eccentricity. If the system had started with an eccentric orbit, it would still exhibit significant eccentricity at the current age. This indicates that either the system must have started with a very low eccentricity before entering the AGB phase, or tidal circularisation is even stronger then currently predicted during the evolved phases (see main text).

Data availability Standard ALMA pipeline products and the enhanced products and scripts for 2018.1.00659.L are available via the ALMA Science Archive. The ALMA data from the proposal 2023.1.00091.S can be retrieved from the ALMA data archive at http://almascience.eso.org/aq/. Other ALMA products, including molecular line maps, will be made available on reasonable request by sending a request to A.M.S. Richards (a.m.s.richards@manchester.ac.uk).

Code availability The scripts used to generate all figures in the main paper, Methods section, and Supplementary Information are available upon request. For specific components, please contact:

- Mats Esseldeurs (mats.esseldeurs@kuleuven.be) for 3D hydrodynamical simulations and orbital evolution calculations,
- Leen Decin (leen.decin@kuleuven.be) for Bayesian retrieval of the orbital parameters,
- Anita M. S. Richards (a.m.s.richards@manchester.ac.uk) for ALMA data reduction, and
- Amanda I. Karakas (amanda.karakas@monash.edu) for stellar evolution calculations.

PHANTOM is publicly available at https://github.com/danieljprice/phantom. PLONS is publicly available at https://github.com/Ensor-code/plons.

Acknowledgments This papers uses the ALMA data ADS/JAO.ALMA2018.1.00659.L, 'ATOMIUM: ALMA tracing the origins of molecules forming dust in oxygen-rich M-type stars' and ADS/JAO.ALMA. 2023.1.00091.S, 'Putting to test the first hypothesized ALMA detections of a close stellar/planetary companion orbiting an AGB star'. ALMA is a partnership of ESO (representing its member states), NSF (USA) and NINS (Japan), together with NRC (Canada) and NSC and ASIAA (Taiwan), in cooperation with the Republic of Chile. The Joint ALMA Observatory is operated by ESO, auI/NRAO and NAOJ. This paper makes use of the CASA data reduction package: http://casa.nra.edu - Credit: International consortium of scientists based at the National Radio Astronomical Observatory (NRAO), the European Southern Observatory (ESO), the National Astronomical Observatory of Japan (NAOJ), the CSIRO Australia Telescope National Facility (CSIRO/ATNF), and the Netherlands Institute for Radio Astronomy (ASTRON) under the guidance of NRAO. The authors thanks the Data Reduction team at ESO for customizing the imaging pipeline. This paper makes use of the Cologne Database for Molecular Spectroscopy (CDMS; https://www.astro.uni-koeln.de/cdms/catalog) and the spectral line catalogs of the Jet Propulsion Laboratory (JPL; https://spec.jpl.nasa); This work has made use of data from the European Space Agency (ESA) mission *Gaia* (https://www.cosmos.esa.int/gaia), processed by the *Gaia* Data Processing and Analysis Consortium (DPAC, https://www.cosmos.esa.int/web/gaia/dpac/consortium). Funding for the DPAC has been provided by national institutions, in particular the institutions participating in the *Gaia* Multilateral Agreement. This work made use of the latest *Hipparcos* reduction whose validation is described in Ref. [100]. Computer resources have been provided by the KU Leuven C1 Excellence Grant BRAVE KAC/16/23/008, the VSC Flemish supercomputer, and STFC IRIS. The consortium thanks Hans Van Winckel, Graham Harper and Pat Wallace for useful discussions. M.E. acknowledges funding from the FWO research grants G099720N and G0B3823N. L.D. acknowledges support from the KU Leuven C1 excellence grant BRAVE C16/23/009, KU Leuven Methusalem grant SOUL METH/24/012, and the FWO research grants G099720N and G0B3823N. Y.M, A.I.K, T.D., Z.O. acknowledge this research is supported in part by the Australian Research Council Centre of Excellence

for All Sky Astrophysics in 3 Dimensions (ASTRO 3D), through project number CE170100013. J.M. acknowledges support from the FWO research grant G099720N. T.D. is supported in part by the Australian Research Council through a Discovery Early Career Researcher Award (DE230100183). S.M. acknowledges support from the European Research Council (ERC) under the Horizon Europe programme (Synergy Grant agreement 101071505: 4D-STAR), from the CNES SOHO-GOLF and PLATO grants at CEA-DAp, and from PNPS (CNRS/INSU). While partially funded by the European Union, views and opinions expressed are however those of the author only and do not necessarily reflect those of the European Union or the European Research Council. Neither the European Union nor the granting authority can be held responsible for them. R.S.'s contribution to the research described here was carried out at the Jet Propulsion Laboratory, California Institute of Technology, under a contract with NASA, and funded in part by NASA via ADAP award number 80NM0018F0610. M.V.d.S. acknowledges support from the Oort Fellowship at Leiden Observatory. T.C. acknowledges funding from the Research Foundation - Flanders (FWO), grant 1166724N. F.D.C. is a Postdoctoral Research Fellow of the Research Foundation - Flanders (FWO), grant 1253223N. I.E.M. acknowledges support from ANID/FONDECYT, grant 11240206. This work is funded by the French National Research Agency (ANR) project PEPPER (ANR-20-CE31-0002). P.K. acknowledges funding from the European Research Council (ERC) under the European Union's Horizon 2020 research and innovation program (project UniverScale, grant agreement 951549). C.L. acknowledges support from the KU Leuven C1 excellence grant BRAVE C16/23/009. T.J.M. acknowledges support from STFC grant no. ST/T000198/1. J.M.C.P. acknowledges support for the UKRI STFC grant ST/T000287/1. Z.O. acknowledges this research was supported by an Australian Government Research Training Program (RTP) Scholarship. D.J.P. acknowledges Australian Research Council funding via DP220103767. We also thank the Australia French Association for Research and Innovation (AFRAN) for financially supporting the 5th Phantom users workshop. L.S. is FNRS senior researcher. O.V. acknowledges funding from the Research Foundation - Flanders (FWO), grant 1173025N. K.T.W. acknowledges support from the European Research Council (ERC) under the European Union's Horizon 2020 Research and Innovation programme (grant agreement number 883867, project EXWINGS).

Author Contributions L.D. is PI of the ALMA Large Program ATOMIUM 2018.1.000659.L and PI of the ALMA Program 2023.1.00091.S, developed the orbital model, developed and executed the Bayesian methodology to retrieve the orbital parameters, and derived the properties of π^1 Gru C and its accretion disk. M.E. and S.M. computed the tidal effects and the orbital evolution of the system. J.M. and M.E. computed the 3D hydrodynamical simulations of the binary system. A.M.S.R. led the ALMA data reduction and wrote software used in the data reduction. J.D.R. advised in the development of the orbital model and Bayesian retrieval framework. A.I.K. and Y.M. computed the initial mass of π^1 Gru A and its stellar evolution. R.S. advised in the derivation of the properties of the accretion disk. L.S. advised in the calculations of the orbital evolution. T.D. and I.M.D advised in the inclusion of the ALMA parallax shift. M.V.d.S and T.D. advised on the discussion of the chemical signature of the companion. P.K. has contributed to the astrometry and quantification of the proper motion anomaly. All authors discussed the interpretation of the data, contributed to the scientific results, and helped prepare the paper.

Author Information ⋆ Correspondence and requests for materials should be addressed to mats.esseldeurs@kuleuven.be and/or leen.decin@kuleuven.be.

Competing Interests The authors declare that they have no competing interests.

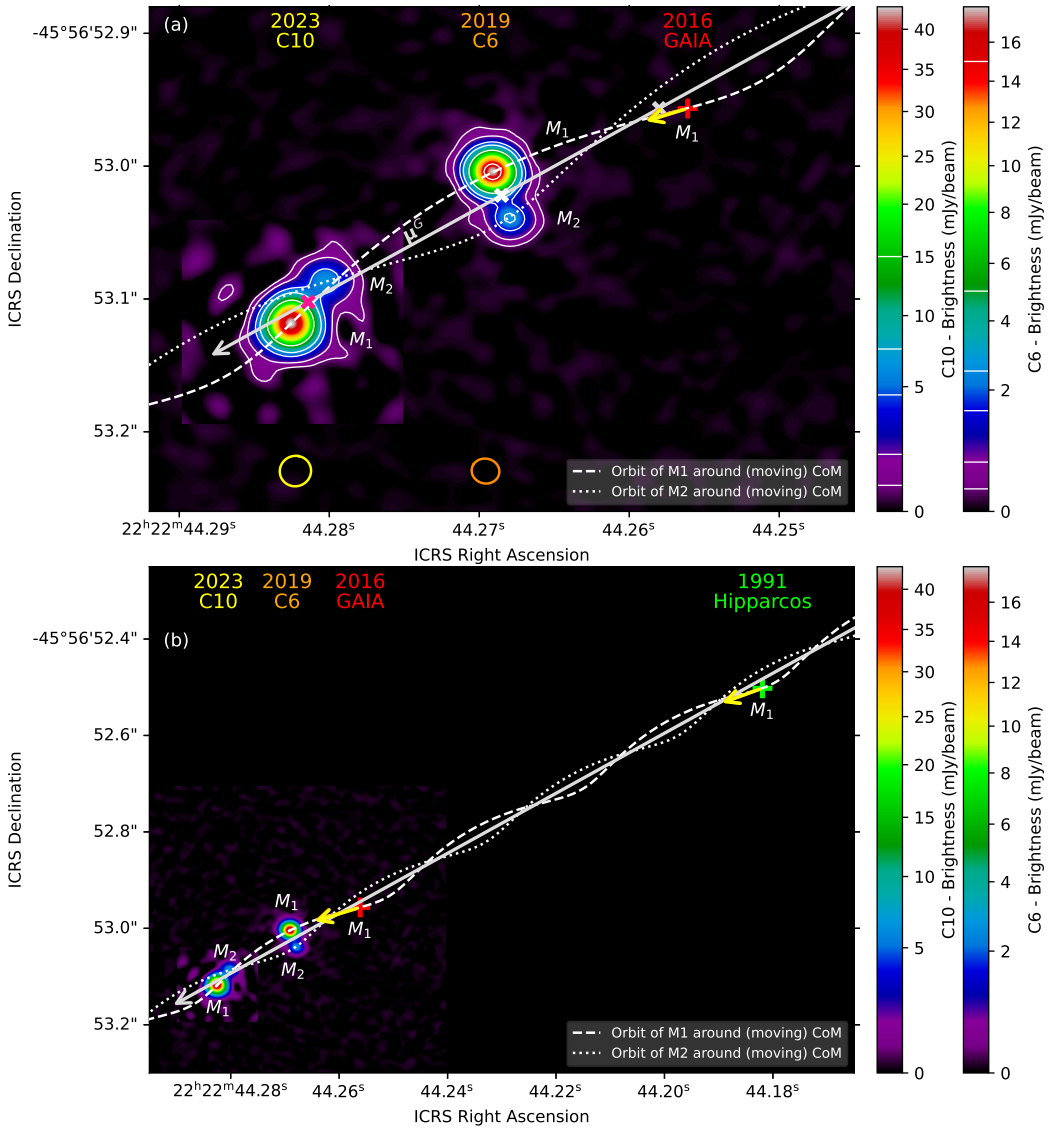

Figure 1: **Proper motion of the π^1 Gru system.** Panel (a): 2019 ALMA C6 and 2023 ALMA C10 data with white contours at (3, 10, 30, 50, 100, 300)$\times$ the continuum rms value. The ALMA beam sizes are shown in orange (2019 C6) and yellow (2023 C10) at the bottom. Data are corrected for the parallactic shift. The red cross marks the *Gaia* 2016.0 position of π^1 Gru A. The grey arrow (μ^G) indicates the proper motion of the binary system's center of mass (CoM, $G_\star$). The white, pink, and grey crosses mark the barycentre's position at the 2019, 2023, and *Gaia* 2016.0 epochs, respectively. The dashed white line shows the orbit of π^1 Gru A (M_1), while the dotted white line shows the orbit of π^1 Gru C (M_2), both in the ICRS frame based on Bayesian best-fit parameters. Panel (b): Similar to (a), but also including the *Hipparcos* 1991.25 position of π^1 Gru A (green cross). ALMA contour levels are omitted for clarity. In both panels, observed proper motion is in yellow, predicted motion in orange, with vectors representing 1-year (panel a) and 3-year (panel b) intervals. The orange vector is nearly indistinguishable due to the almost perfect fit with the observed motion. An accompanying video is in Suppl. Video 1.

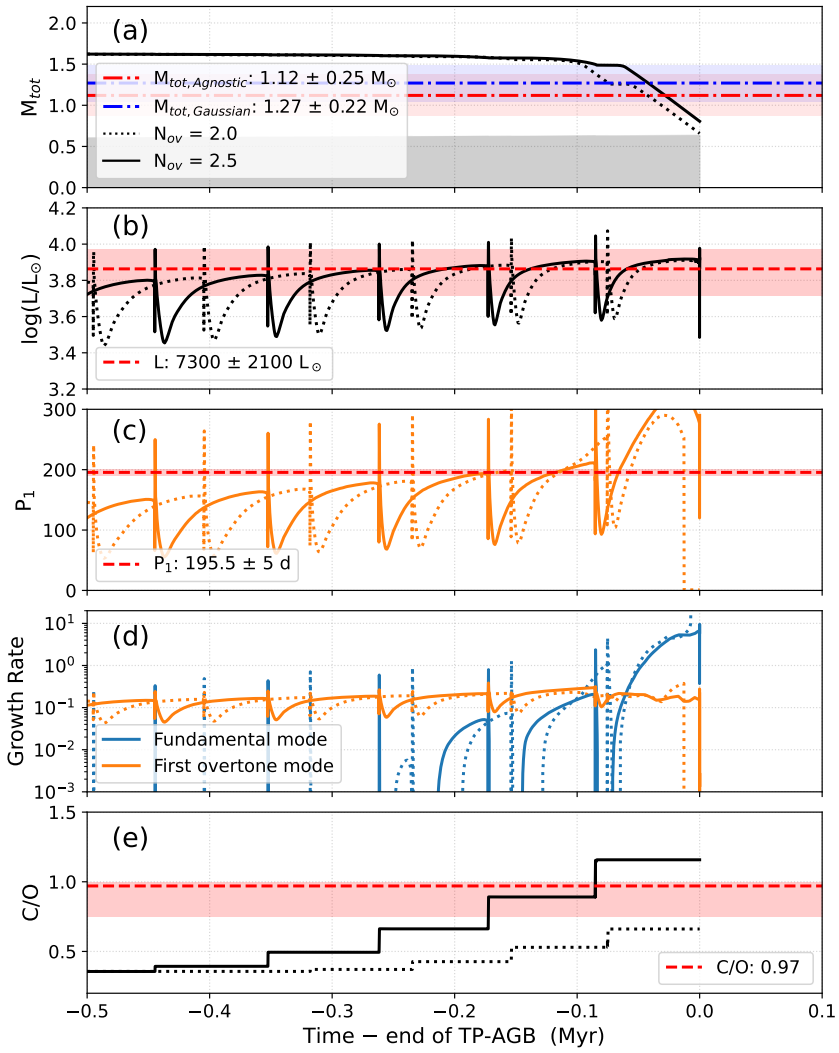

Figure 2: **Time evolution of stellar parameters for a 1.7 $M_\odot$ model near the end of the thermally-pulsing AGB, compared to observed values for π^1 Gru A.** We include models with two different values for the overshoot parameter in pressure scale heights, $N_{\rm ov}$, of 2.0 (dotted lines) and 2.5 (solid lines). The panels show from top to bottom: (a): total (lines) and core masses (grey shaded region), (b): luminosity, (c): first overtone mode period, (d): amplitude growth rates for the first overtone mode (orange) and fundamental mode (blue) and (e): C/O ratio; all with respect to time since the onset of the TP-AGB phase. Also included are the measurements for π^1 Gru A (red dashed lines and shaded regions): luminosity of 7,300 $L_\odot$, period of 195.5 d and C/O ratio of 0.97 (between 0.75 and 1). In the top panel, we plot the derived masses from both agnostic and Gaussian priors on m_1, which are 1.12 and 1.27 $M_\odot$ respectively. The period, luminosity and total mass are consistent with the final few thermal pulses of this model, though the higher mass using the Gaussian prior is favoured for this model mass. The first overtone mode is also dominant at these model times (i.e. the growth rate is higher), which is consistent with the observed pulsation mode of π^1 Gru A.

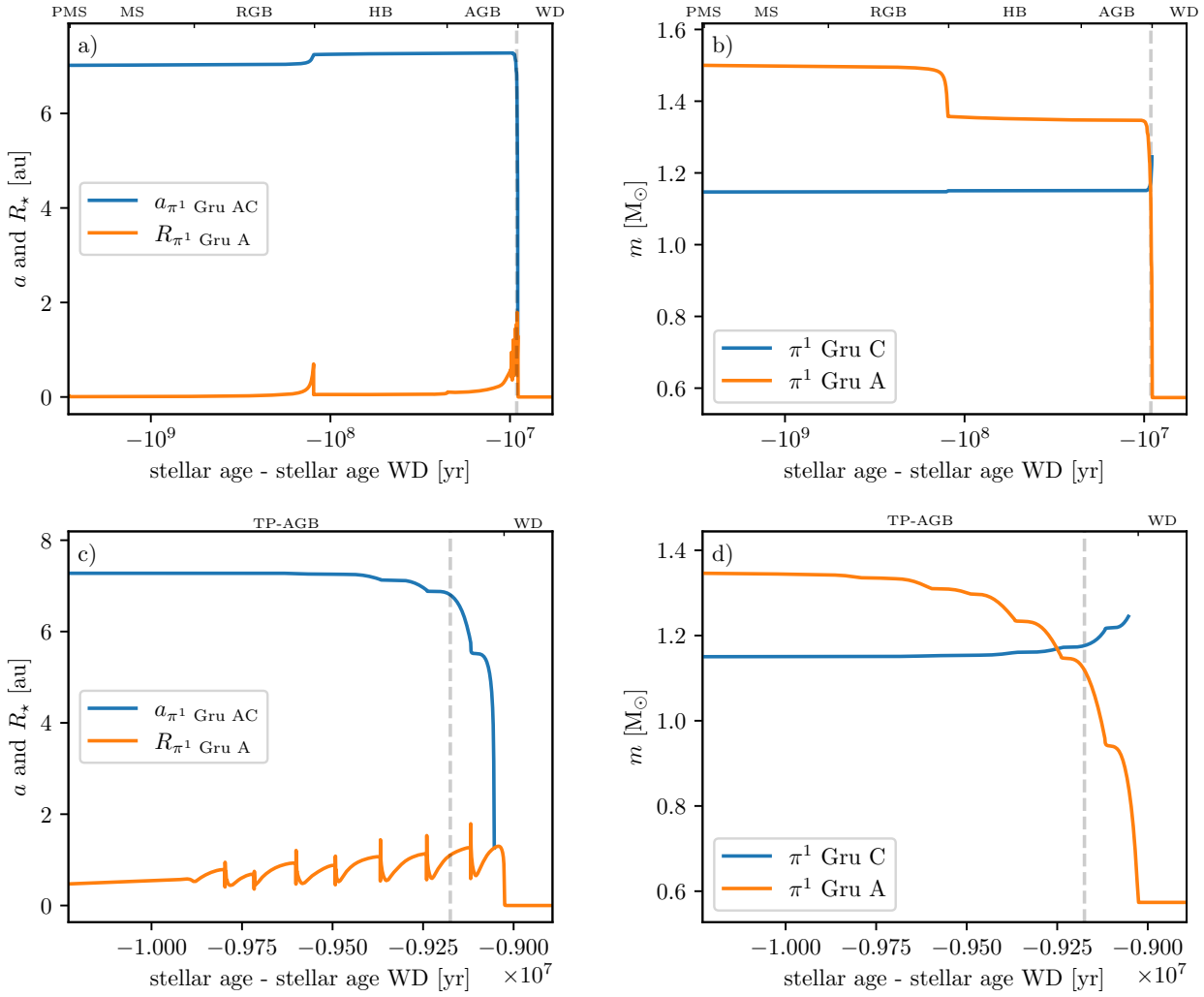

Figure 3: **Orbital evolution of the π^1 Gru system during the TP-AGB phase.** Panel (a) illustrates the variation in orbital separation a over time (blue line), along with the evolution of the radius of π^1 Gru A (orange line). Panel (b) shows the mass evolution of π^1 Gru A (orange line) and π^1 Gru C (blue line). Panels (c) and (d) show a zoom-in to the TP-AGB phase. These panels show the evolution of the system parameters when the initial mass of π^1 Gru A is set to 1.5 $M_\odot$, and the current mass of π^1 Gru C is set to 1.12 $M_\odot$. Initially, the system has a mass ratio $q < 1$, but mass loss from π^1 Gru A and mass accretion onto π^1 Gru C lead to an increase, resulting in $q > 1$. For clarity on the timescale, the x-axis represents "stellar age – stellar age WD [yr]", where "stellar age WD" indicates the age at which the white dwarf (WD) has cooled to a luminosity of 10^{-1} $L_\odot$. The vertical dashed grey line in each panel marks the current age of the π^1 Gru system.

References

1. Moe, M. & Di Stefano, R. Mind Your Ps and Qs: The Interrelation between Period (P) and Mass-ratio (Q) Distributions of Binary Stars. *Astrophys. J. Suppl.* **230**, 15 (2017).

2. Decin, L. *et al.* (Sub)stellar companions shape the winds of evolved stars. *Science* **369**, 1497–1500 (2020).

3. Kroupa, P. On the variation of the initial mass function. *Mon. Not. Roy. Astron. Soc.* **322**, 231–246 (2001).

4. Veras, D. Post-main-sequence planetary system evolution. *Royal Society Open Science* **3**, 150571 (2016).

5. Saladino, M. I., Pols, O. R. & Abate, C. Slowly, slowly in the wind. 3D hydrodynamical simulations of wind mass transfer and angular-momentum loss in AGB binary systems. *Astron. Astrophys.* **626**, A68 (2019).

6. Aydi, E. & Mohamed, S. 3D models of the circumstellar environments of evolved stars: Formation of multiple spiral structures. *Mon. Not. Roy. Astron. Soc.* **513**, 4405–4430 (2022).

7. Van de Sande, M. & Millar, T. J. The impact of stellar companion UV photons on the chemistry of the circumstellar environments of AGB stars. *Mon. Not. Roy. Astron. Soc.* **510**, 1204–1222 (2022).

8. Esseldeurs, M., Mathis, S. & Decin, L. Tidal dissipation in evolved low- and intermediate-mass stars. *Astron. Astrophys.* **690**, A266 (2024).

9. Mayor, M. & Queloz, D. A Jupiter-mass companion to a solar-type star. *Nature* **378**, 355–359 (1995).

10. Maund, J. R., Smartt, S. J., Kudritzki, R. P., Podsiadlowski, P. & Gilmore, G. F. The massive binary companion star to the progenitor of supernova 1993J. *Nature* **427**, 129–131 (2004).

11. Sana, H. *et al.* Binary Interaction Dominates the Evolution of Massive Stars. *Science* **337**, 444 (2012).

12. David, T. J. *et al.* A Neptune-sized transiting planet closely orbiting a 5-10-million-year-old star. *Nature* **534**, 658–661 (2016).

13. Grunblatt, S. K. *et al.* K2-97b: A (Re-?)Inflated Planet Orbiting a Red Giant Star. *Astron. J.* **152**, 185 (2016).

14. Decin, L. Evolution and Mass Loss of Cool Ageing Stars: a Daedalean Story. *Ann. Rev. Astron. Astrophys.* **59**, 337–389 (2021).

15. Sahai, R. *et al.* Binarity and Accretion in AGB Stars: HST/STIS Observations of UV Flickering in Y Gem. *Astrophys. J.* **860**, 105 (2018).

16. Soszyński, I. *et al.* Binarity as the Origin of Long Secondary Periods in Red Giant Stars. *Astrophys. J. Lett.* **911**, L22 (2021).

17. Hinkle, K. H., Fekel, F. C. & Joyce, R. R. Infrared Spectroscopy of Symbiotic Stars. VII. Binary Orbit and Long Secondary Period Variability of CH Cygni. *Astrophys. J.* **692**, 1360–1373 (2009).

18. Planquart, L., Jorissen, A., Escorza, A., Verhamme, O. & Van Winckel, H. A dynamic view of V Hydrae. Monitoring of a spectroscopic-binary AGB star with an alkaline jet. *Astron. Astrophys.* **682**, A143 (2024).

19. Kiss, L. L., Szabó, G. M. & Bedding, T. R. Variability in red supergiant stars: pulsations, long secondary periods and convection noise. *Mon. Not. Roy. Astron. Soc.* **372**, 1721–1734 (2006).

20. Salas, J. M., Naoz, S., Morris, M. R. & Stephan, A. P. Unseen companions of V Hya inferred from periodic ejections. *Mon. Not. Roy. Astron. Soc.* **487**, 3029–3036 (2019).

21. Alcolea, J. *et al.* Determining the orbital parameters of binary systems with an AGB primary. The case of the R Aqr symbiotic system. In Manteiga, M. *et al.* (eds.) *Highlights on Spanish Astrophysics XI*, 190 (2023).

22. Karovska, M., Hack, W., Raymond, J. & Guinan, E. First Hubble Space Telescope Observations of Mira AB Wind-accreting Binary Systems. *Astrophys. J. Lett.* **482**, L175–L178 (1997).

23. Danilovich, T. *et al.* Chemical tracers of a highly eccentric AGB-main-sequence star binary. *Nature Astronomy* **8**, 308–327 (2024).

24. Kervella, P. *et al.* ALMA observations of the nearby AGB star L_2 Puppis. I. Mass of the central star and detection of a candidate planet. *Astron. Astrophys.* **596**, A92 (2016).

25. Homan, W. *et al.* ATOMIUM: A high-resolution view on the highly asymmetric wind of the AGB star π^1Gruis. I. First detection of a new companion and its effect on the inner wind. *Astron. Astrophys.* **644**, A61 (2020).

26. Doan, L. *et al.* The extended molecular envelope of the asymptotic giant branch star π^1 Gruis as seen by ALMA. II. The spiral-outflow observed at high-angular resolution. *Astron. Astrophys.* **633**, A13 (2020).

27. Chiu, P.-J. *et al.* A Slowly Expanding Disk and Fast Bipolar Outflow from the S Star π^1 Gruis. *Astrophys. J.* **645**, 605–612 (2006).

28. Mayer, A. *et al.* Large-scale environments of binary AGB stars probed by Herschel. II. Two companions interacting with the wind of π^1 Gruis. *Astron. Astrophys.* **570**, A113 (2014).

29. Montargès, M. *et al.* An accreting dwarf star orbiting the S-type giant star π^1 Gru. *Astron. Astrophys.* **699**, A22 (2025).

30. Feast, M. W. The absolute magnitude and spectrum of the class S star π^1 Gruis. *Mon. Not. Roy. Astron. Soc.* **113**, 510 (1953).

31. Mohamed, S. & Podsiadlowski, P. Wind Roche-Lobe Overflow: a New Mass-Transfer Mode for Wide Binaries. In Napiwotzki, R. & Burleigh, M. R. (eds.) *15th European Workshop on White Dwarfs*, vol. 372 of *Astronomical Society of the Pacific Conference Series*, 397 (2007).

32. Siess, L., Homan, W., Toupin, S. & Price, D. J. 3D simulations of AGB stellar winds. I. Steady winds and dust formation. *Astron. Astrophys.* **667**, A75 (2022).

33. Malfait, J. *et al.* Impact of H I cooling and study of accretion disks in asymptotic giant branch wind-companion smoothed particle hydrodynamic simulations. *Astron. Astrophys.* **691**, A84 (2024).

34. O'Gorman, E. *et al.* ALMA observations of anisotropic dust mass loss in the inner circumstellar environment of the red supergiant VY Canis Majoris. *Astron. Astrophys.* **573**, L1 (2015).

35. Karakas, A. I. Helium enrichment and carbon-star production in metal-rich populations. *Mon. Not. Roy. Astron. Soc.* **445**, 347–358 (2014).

36. Tabur, V. *et al.* Long-term photometry and periods for 261 nearby pulsating M giants. *Mon. Not. Roy. Astron. Soc.* **400**, 1945–1961 (2009).

37. Trabucchi, M. *et al.* Modelling long-period variables - I. A new grid of O-rich and C-rich pulsation models. *Mon. Not. Roy. Astron. Soc.* **482**, 929–949 (2019).

38. Izzard, R. G., Dermine, T. & Church, R. P. White-dwarf kicks and implications for barium stars. *Astron. Astrophys.* **523**, A10 (2010).

39. van Winckel, H. Post-AGB Stars. *Ann. Rev. Astron. Astrophys.* **41**, 391–427 (2003).

40. Meibom, S. & Mathieu, R. D. A Robust Measure of Tidal Circularization in Coeval Binary Populations: The Solar-Type Spectroscopic Binary Population in the Open Cluster M35. *Astrophys. J.* **620**, 970–983 (2005).

41. Nie, J. D., Wood, P. R. & Nicholls, C. P. The Orbital Nature of 81 Ellipsoidal Red Giant Binaries in the Large Magellanic Cloud. *Astrophys. J.* **835**, 209 (2017).

42. Dewberry, J. W. & Wu, Y. Testing Tidal Theory Using Gaia Binaries: The Red Giant Branch. *Astrophys. J.* **984**, 137 (2025).

43. Witte, M. G. & Savonije, G. J. Tidal evolution of eccentric orbits in massive binary systems. A study of resonance locking. *Astron. Astrophys.* **350**, 129–147 (1999).

44. Bergeron, P. *et al.* On the Measurement of Fundamental Parameters of White Dwarfs in the Gaia Era. *Astrophys. J.* **876**, 67 (2019).

45. Mondal, A. *et al.* Optical spectroscopy of the recurrent nova RS Ophiuchi - from the outburst of 2006 to quiescence. *Mon. Not. Roy. Astron. Soc.* **474**, 4211–4224 (2018).

46. Montargès, M. *et al.* The VLT/SPHERE view of the ATOMIUM cool evolved star sample. I. Overview: Sample characterization through polarization analysis. *Astron. Astrophys.* **671**, A96 (2023).

47. Schmid, H. M. *et al.* SPHERE/ZIMPOL observations of the symbiotic system R Aquarii. I. Imaging of the stellar binary and the innermost jet clouds. *Astron. Astrophys.* **602**, A53 (2017).

48. Gottlieb, C. A. *et al.* ATOMIUM: ALMA tracing the origins of molecules in dust forming oxygen rich M-type stars. Motivation, sample, calibration, and initial results. *Astron. Astrophys.* **660**, A94 (2022).

49. Martí-Vidal, I., Vlemmings, W. H. T., Muller, S. & Casey, S. UVMULTIFIT: A versatile tool for fitting astronomical radio interferometric data. *A&A* **563**, A136 (2014).

50. Cortes, P. C. *et al. ALMA Technical Handbook*. ALMA, https://almascience.org/documents-and-tools (2023).

51. Kozai, Y. Secular perturbations of asteroids with high inclination and eccentricity. *Astron. J.* **67**, 591–598 (1962).

52. Lidov, M. L. The evolution of orbits of artificial satellites of planets under the action of gravitational perturbations of external bodies. *Planetary & Space Science* **9**, 719–759 (1962).

53. Li, G., Naoz, S., Kocsis, B. & Loeb, A. Eccentricity Growth and Orbit Flip in Near-coplanar Hierarchical Three-body Systems. *Astrophys. J.* **785**, 116 (2014).

54. Gaia Collaboration *et al.* Gaia Data Release 3. Summary of the content and survey properties. *Astron. Astrophys.* **674**, A1 (2023).

55. Bailer-Jones, C. A. L. Estimating Distances from Parallaxes. *Pub. Astron. Soc. Pacific* **127**, 994 (2015).

56. Buchner, J. UltraNest - a robust, general purpose Bayesian inference engine. *The Journal of Open Source Software* **6**, 3001 (2021).

57. Doan, L. *et al.* The extended molecular envelope of the asymptotic giant branch star π^1 Gruis as seen by ALMA. I. Large-scale kinematic structure and CO excitation properties. *Astron. Astrophys.* **605**, A28 (2017).

58. Eggleton, P. *Evolutionary Processes in Binary and Multiple Stars* (Cambridge University Press, 2006).

59. Hoyle, F. & Lyttleton, R. A. The effect of interstellar matter on climatic variation. *Proceedings of the Cambridge Philosophical Society* **35**, 405 (1939).

60. Bondi, H. & Hoyle, F. On the mechanism of accretion by stars. *Mon. Not. Roy. Astron. Soc.* **104**, 273 (1944).

61. Kim, H. & Taam, R. E. Wide Binary Effects on Asymmetries in Asymptotic Giant Branch Circumstellar Envelopes. *Astrophys. J.* **759**, 59 (2012).

62. Maes, S. *et al.* SPH modelling of companion-perturbed AGB outflows including a new morphology classification scheme. *Astron. Astrophys.* **653**, A25 (2021).

63. Price, D. J. *et al.* Phantom: A Smoothed Particle Hydrodynamics and Magnetohydrodynamics Code for Astrophysics. *Publications of the Astronomical Society of Australia* **35**, e031 (2018).

64. Esseldeurs, M. *et al.* 3D simulations of AGB stellar winds. II. Ray-tracer implementation and impact of radiation on the outflow morphology. *Astron. Astrophys.* **674**, A122 (2023).

65. Jayasinghe, T. *et al.* The ASAS-SN catalogue of variable stars - V. Variables in the Southern hemisphere. *Mon. Not. Roy. Astron. Soc.* **491**, 13–28 (2020).

66. Ducati, J. R. VizieR Online Data Catalog: Catalogue of Stellar Photometry in Johnson's 11-color system. *CDS/ADC Collection of Electronic Catalogues, 2237, 0 (2002)* (2002).

67. Cardelli, J. A., Clayton, G. C. & Mathis, J. S. The Relationship between Infrared, Optical, and Ultraviolet Extinction. *Astrophys. J.* **345**, 245 (1989).

68. Massey, P. *et al.* The Reddening of Red Supergiants: When Smoke Gets in Your Eyes. *Astrophys. J.* **634**, 1286–1292 (2005).

69. Gordon, K. D. *et al.* One Relation for All Wavelengths: The Far-ultraviolet to Mid-infrared Milky Way Spectroscopic R(V)-dependent Dust Extinction Relationship. *Astrophys. J.* **950**, 86 (2023).

70. Bessell, M. S. & Wood, P. R. A note on bolometric corrections for late-type stars and long-period variables. *Pub. Astron. Soc. Pacific* **96**, 247–249 (1984).

71. Paladini, C. *et al.* Large granulation cells on the surface of the giant star π^1 Gruis. *Nature* **553**, 310–312 (2018).

72. Van Eck, S. & Jorissen, A. The Henize sample of S stars. I. The technetium dichotomy. *Astron. Astrophys.* **345**, 127–136 (1999).

73. Murty, P. S. Pi-Gruis - Molecular Identifications and Spectral Classification. *Astrophys. and Space Science* **94**, 295–305 (1983).

74. Karakas, A. I. & Lattanzio, J. C. The Dawes Review 2: Nucleosynthesis and Stellar Yields of Low- and Intermediate-Mass Single Stars. *PASA* **31**, e030 (2014).

75. Kamath, D., Karakas, A. I. & Wood, P. R. Evolution and Nucleosynthesis of Asymptotic Giant Branch Stars in Three Magellanic Cloud Clusters. *Astrophys. J.* **746**, 20 (2012).

76. Schröder, K. P. & Cuntz, M. A New Version of Reimers' Law of Mass Loss Based on a Physical Approach. *Astrophys. J. Lett.* **630**, L73–L76 (2005).

77. Watson, C. L., Henden, A. A. & Price, A. The International Variable Star Index (VSX). *Society for Astronomical Sciences Annual Symposium* **25**, 47 (2006).

78. Pojmanski, G. The All Sky Automated Survey. Catalog of Variable Stars. I. 0 h - 6 hQuarter of the Southern Hemisphere. *Acta Astronomica* **52**, 397–427 (2002).

79. Kochanek, C. S. *et al.* The All-Sky Automated Survey for Supernovae (ASAS-SN) Light Curve Server v1.0. *Pub. Astron. Soc. Pacific* **129**, 104502 (2017).

80. Trabucchi, M. *et al.* A New Interpretation of the Period-Luminosity Sequences of Long-period Variables. *Astrophys. J.* **847**, 139 (2017).

81. Soszyński, I. *et al.* The Optical Gravitational Lensing Experiment. The OGLE-III Catalog of Variable Stars. IV. Long-Period Variables in the Large Magellanic Cloud. *Acta Astronomica* **59**, 239–253 (2009).

82. Christy, C. T. *et al.* The ASAS-SN catalogue of variable stars X: discovery of 116 000 new variable stars using G-band photometry. *Mon. Not. Roy. Astron. Soc.* **519**, 5271–5287 (2023).

83. de Grijs, R. *et al.* Toward an Internally Consistent Astronomical Distance Scale. *Space Science Rev.* **212**, 1743–1785 (2017).

84. Bailer-Jones, C. A. L., Rybizki, J., Fouesneau, M., Demleitner, M. & Andrae, R. Estimating Distances from Parallaxes. V. Geometric and Photogeometric Distances to 1.47 Billion Stars in Gaia Early Data Release 3. *Astron. J.* **161**, 147 (2021).

85. Trabucchi, M., Mowlavi, N. & Lebzelter, T. Semi-regular red giants as distance indicators. I. The period-luminosity relations of semi-regular variables revisited. *Astron. Astrophys.* **656**, A66 (2021).

86. Whitelock, P. A., Feast, M. W. & Van Leeuwen, F. AGB variables and the Mira period-luminosity relation. *Mon. Not. Roy. Astron. Soc.* **386**, 313–323 (2008).

87. Trabucchi, M. & Pastorelli, G. Self-excited Pulsations and the Instability Strip of Long-period Variables: The Transition from Small-amplitude Red Giants to Semi-regular Variables. *Astrophys. J.* **978**, 30 (2025).

88. Andriantsaralaza, M., Ramstedt, S., Vlemmings, W. H. T. & De Beck, E. Distance estimates for AGB stars from parallax measurements. *Astron. Astrophys.* **667**, A74 (2022).

89. Siess, L., Izzard, R. G., Davis, P. J. & Deschamps, R. BINSTAR: a new binary stellar evolution code. Tidal interactions. *Astron. Astrophys.* **550**, A100 (2013).

90. Hurley, J. R., Tout, C. A. & Pols, O. R. Evolution of binary stars and the effect of tides on binary populations. *Mon. Not. Roy. Astron. Soc.* **329**, 897–928 (2002).

91. Dosopoulou, F. & Kalogera, V. Orbital Evolution of Mass-transferring Eccentric Binary Systems. II. Secular Evolution. *Astrophys. J.* **825**, 71 (2016).

92. Saladino, M. I. & Pols, O. R. The eccentric behaviour of windy binary stars. *Astron. Astrophys.* **629**, A103 (2019).

93. Fuller, J., Piro, A. L. & Jermyn, A. S. Slowing the spins of stellar cores. *Mon. Not. Roy. Astron. Soc.* **485**, 3661–3680 (2019).

94. Ogilvie, G. I. Tidal Dissipation in Stars and Giant Planets. *Ann. Rev. Astron. Astrophys.* **52**, 171–210 (2014).

95. Mathis, S. & Le Poncin-Lafitte, C. Tidal dynamics of extended bodies in planetary systems and multiple stars. *Astron. Astrophys.* **497**, 889–910 (2009).

96. Smeyers, P., van Hout, M., Ruymaekers, E. & Polfliet, R. Effects of dynamic tides on the rate of apsidal motion in close binary systems. *Astron. Astrophys.* **248**, 94–104 (1991).

97. Zahn, J. P. Les marées dans une étoile double serrée. *Annales d'Astrophysique* **29**, 313 (1966).

98. Jermyn, A. S. *et al.* Modules for Experiments in Stellar Astrophysics (MESA): Time-dependent Convection, Energy Conservation, Automatic Differentiation, and Infrastructure. *Astrophys. J. Suppl.* **265**, 15 (2023).

99. Cinquegrana, G. C., Joyce, M. & Karakas, A. I. Bridging the Gap between Intermediate and Massive Stars. I. Validation of MESA against the State-of-the-Art Monash Stellar Evolution Program for a 2M $_\odot$ AGB Star. *Astrophys. J.* **939**, 50 (2022).

100. van Leeuwen, F. Validation of the new Hipparcos reduction. *Astron. Astrophys.* **474**, 653–664 (2007).